CHALMERS
UNIVERSITY OF TECHNOLOGY

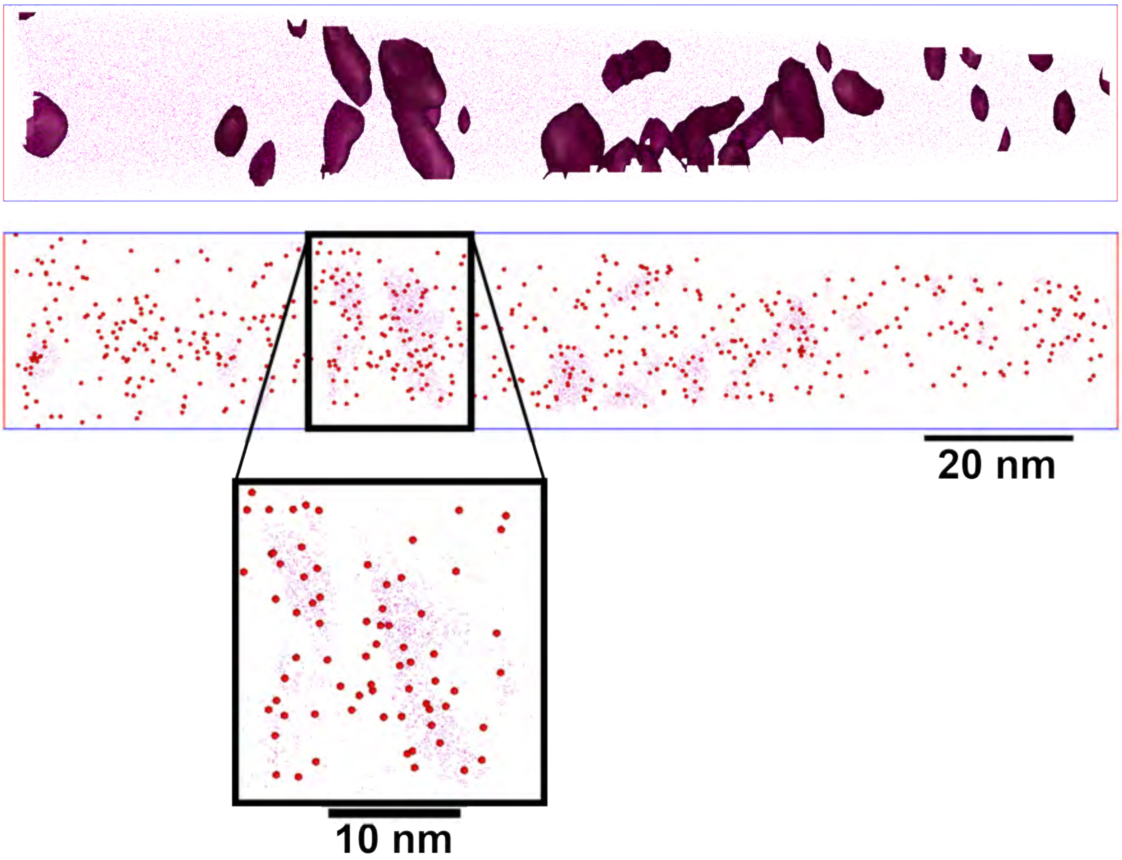

Experimental study of hydrogen trapping by carbides in low alloyed steels using Atom Probe Tomography

Master's thesis for the Double Degree in Materials Engineering and Materials Science submitted to the Chalmers University of Technology and the University of Stuttgart

MORITZ LUDWIG

DEPARTMENT OF PHYSICS
CHALMERS UNIVERSITY OF TECHNOLOGY
Gothenburg, Sweden 2024
www.chalmers.se

Master's thesis 2024

Experimental study of hydrogen trapping by carbides in low alloyed steels using Atom Probe Tomography

MORITZ LUDWIG

Department of Physics
Division of Microstructure Physics
Chalmers University of Technology
Gothenburg, Sweden 2024

Experimental study of hydrogen trapping by carbides in low alloyed steels using Atom Probe Tomography
MORITZ LUDWIG

Supervisor: Dr. Severin Jakob
Examiner (Chalmers): Assoc. Prof. Dr. Mattias Thuvander
Examiner (Stuttgart): Prof. Dr. Dr. h.c. Guido Schmitz

Master's Thesis 2024
Department of Physics
Division of Microstructure Physics
Chalmers University of Technology
SE-412 96 Gothenburg
Telephone +46 31 772 1000

Cover: Overview of a V-steel sample, illustrating D trapping within the V carbide. In the first image, Fe atoms are depicted in pink, while the isosurfaces representing a combined concentration of (C, Mo, V) >3.4 at.% are shown in brown. The second image highlights the V (pink) and D (red) atoms. The third image presents a 10 nm slice.

Typeset in LaTeX
Printed by Chalmers Reproservice
Gothenburg, Sweden 2024

Author declaration

I declare that the enclosed thesis was entirely developed and written by me. All sources and means are declared in the text, and any external ideas or direct quotations are distinctly marked. This thesis has not been submitted for academic grading or published elsewhere in any form. The enclosed electronic version is identical to the printed copies.

09.09.2024 M. Ludwig

Date, Signature

Experimental study of hydrogen trapping by carbides in low alloyed steels using Atom Probe Tomography
MORITZ LUDWIG
Department of Physics
Chalmers University of Technology

Abstract

Hydrogen embrittlement (HE) of high-strength low-alloy (HSLA) steels is a big problem. Several options are known to prevent/delay the embrittlement of the steels. One option is to trap the hydrogen at or inside the carbides. This could be interpreted as an energetic interaction, as the nano-sized carbides contribute to the mechanical strength of the material. This work investigates three different low alloyed steels, named in the thesis Steel-1, Ti-steel and V-steel. For the electrochemical D loading process, a 0.1 M NaOH in D_2O is used. The specimens are transferred at room temperature (RT) to the atom probe (AP). Crystallographic calibration was carried out for all measurements. For Steel-1 in the quenched state, no trapping can be seen. For the annealed specimens, the trapping capability can be argued. The Ti- and V-steel show D trapping. Besides the standard measurement, a *room temperature degassing* experiment was carried out for the Ti- and V-steel to get a qualitative insight into the strength of the traps.

Keywords: Atom Probe Tomography, Hydrogen Embrittlement, High-strength low-alloy steel, Hydrogen traps, Carbides

Acknowledgement

I would like to take this opportunity to thank everyone who has supported me during my studies, especially during my Master's thesis.
First of all, I would like to thank my examiner Mattias Thuvander for giving me the opportunity to work on this exciting topic. Thank you for discussing the topic and answering all my questions. I would also like to thank Guido Schmitz for being my examiner at the University of Stuttgart.
I would really like to thank my supervisor Severin Jacob for introducing me to the topic and showing me everything from sample preparation to APT data evaluation. Thank you for always taking the time to answer my questions, the discussions about the topic and the off-topic office discussions.
I want to thank the Chalmers Materials Analysis Laboratory (CMAL) where all the APT measurements where performed. Thanks also to David Mayweg for his expertise and assistance in evaluating the APT data. Special thanks to all members of the Microstructure Physics group for the nice conversations during lunch and fika breaks, it was a great time with you.
A big thanks goes to my family for their support during my studies. My last thanks goes to my girlfriend Mai for supporting me and overcoming the times when I was busy with my thesis and had even less time than normal.

Moritz Ludwig, Gothenburg, July 2024

List of Acronyms

HE	hydrogen embrittlement
IHE	internal hydrogen embrittlement
HEE	hydrogen environment embrittlement
HEDE	hydrogen-enhanced decohesion
HELP	hydrogen-enhanced localised plasticity
AIDE	adsorption-induced dislocation emission
FIM	field ion microscope
APT	atom probe tomography
AP	atom probe
UHV	ultra high vacuum
ICF	image compression factor
HSLA	high-strength low-alloy
GB	grain boundary
RT	room temperature
DR	detection rate
PF	pulse fraction
PR	pulse rate
TDMS	thermal desorption mass spectrometry

Contents

List of Figures

List of Tables

1

Introduction and Aim

The utilization of (green) hydrogen increases to create a more sustainable industry and achieve global sustainability goals [1–3]. To use hydrogen economically, the hydrogen needs to be transported in a cost-effective way. One possibility is to use the existing natural gas infrastructure. The problem of transporting hydrogen in steel pipelines is the hydrogen-induced/mediated embrittlement of the material [4]. It is important for the growing usage of hydrogen in daily life to have more resistant materials against hydrogen embrittlement (HE). One option to achieve this is to trap the diffusible hydrogen. For a suitable trapping, the traps should provide sufficient trapping sites and should be strong enough to prevent the diffusion of hydrogen to critical areas in the material. High-strength low-alloy (HSLA) steel is a promising and cost-effective class of materials. The nano-sized carbides are present in a high number and providing a high surface area. To analyze them, a microscope with high chemical and spatial resolution is required. The atom probe tomography (APT) fulfills the required conditions at that length-scale.

The aim of the thesis is to investigate the hydrogen trapping capability of different carbides in different types of low-alloyed steels using APT.

2

Background

2.1 Hydrogen Embrittlement

HE is a reduction in the ductility and strength of a material caused by the indiffusion of atomic hydrogen into the crystalline lattice of the metal [5]. Some catastrophic failures in the past are connected to HE, like the failure of a high number of anchor rods of the San Francisco-Oakland Bay Bridge in the year 2013 [6]. To prevent such failures, it's important to know how to increase the resistance of steels to HE.

2.1.1 Hydrogen Uptake

In general, different types of HE are known. The different mechanisms have in common that hydrogen has a detrimental effect on material properties and causes premature failure [7]. Hydrogen diffuses as an atomic species into the material [5]. Three possible absorption mechanisms are shown below.

The first mechanism is called *pressurized charging*. The mechanism is shown in Figure 2.1. First, the molecular hydrogen is adsorbed on the metal surface. The cleavage in two hydrogen atoms occurs on the surface, continued by the absorption into the material [8].
The second mechanism is called *electrolytic hydrogen charging* and is connected to corrosion in an acidic environment. Equation 2.1 shows the reduction reaction of the process. The needed electron for the process is supplied by the oxidation of the metal [8].

$$\mathrm{H^+ + e^- \longrightarrow H_{ad} \longleftrightarrow H_{ab}} \tag{2.1}$$

The last mechanism is called *cathodic charging*, the chemical reaction is shown in Equation 2.2. An external potential forces the cleavage of water molecules on the metal surface and create atomic hydrogen [8].

$$\mathrm{H_2O + e^- \longrightarrow H_{ad} + OH^-} \tag{2.2}$$

The *cathodic charging* is later used to load the investigated samples with deuterium. See Section 3.3.

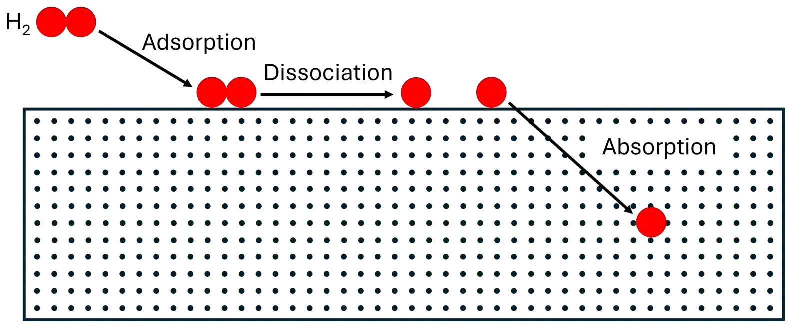

Figure 2.1: Mechanism for the hydrogen absorption directly from the gas phase. Based on [9].

2.1.2 Embrittlement Mechanisms

The absorbed hydrogen diffuses as atoms through the lattice. Sites with increased *residence time* for the hydrogen atoms are called traps. Figure 2.2 shows the possible trapping sites for the atomic as well as for the recombined molecular hydrogen at an atomic and a macroscopic scale [5, 7].

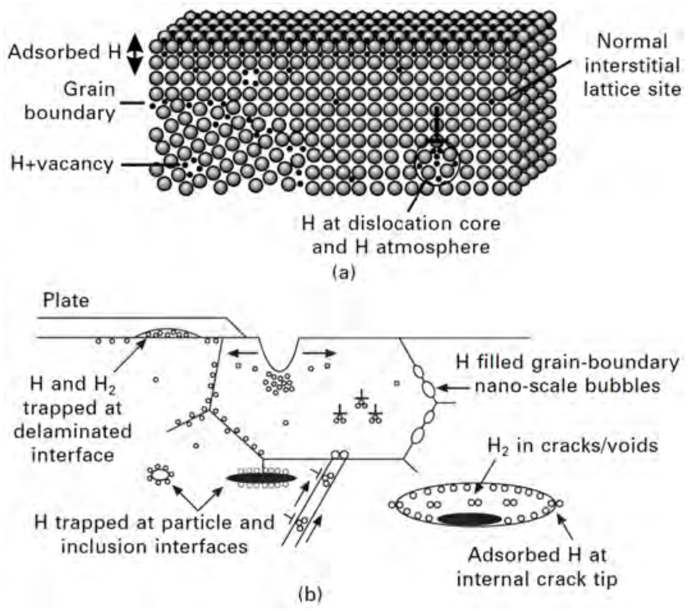

Figure 2.2: Locations for hydrogen inside of materials at an atomic (a) and a macroscopic scale (b). Reprinted from [7],with permission from Elsevier.

HE can be characterized by the origin of the hydrogen. For internal hydrogen embrittlement (IHE), the hydrogen comes from the production process. The hydrogen is then mainly located in regions of high hydrostatic stress in the material, and the cracks occur well below the yield stress. For hydrogen environment embrittlement (HEE), the hydrogen mainly comes from the use of the material in hydrogen-containing environments. There the hydrogen mainly causes sub-critical crack growth and brittle hydride formation at and ahead of the crack tip.

The hydrogen atoms can also recombine in voids or other free volumes to high-pressure molecular hydrogen. This process can induce plastic deformation in the surrounding matrix and lead to crack formation at the interface. This phenomenon is known as *blistering* and can also be seen in Figure 2.2 [7].
The main variables for HE are the affected material itself in terms of composition, microstructure, impurity level and the strength of the material as well as external stresses, hydrogen content, temperature and strain rate [7]. In the following, four possible mechanisms are discussed.

First, the *hydride formation and fracture* theory. The theory is based on the formation of brittle hydrates at crack tips followed by their fracture. Important for this mechanism is the correct temperature at which the hydrogen diffusivity is high enough to reach the crack tip, and the formed metal-hydrides need to be stable [7, 10].
The hydrogen-enhanced decohesion (HEDE) theory is based on the weakening of interatomic bonds through electronic interactions. It is proposed that a high hydrogen concentration is needed for sufficient weakening and cleavage of the bonds. Besides the hydrogen, impurities inside the material can also weaken the matrix bonds [7, 11].
The hydrogen-enhanced localised plasticity (HELP) theory describes the plastification of the material due to hydrogen incorporation. The hydrogen near crack tips increases the mobility of dislocations locally, which supports sub-critical crack growth [7, 12].
The adsorption-induced dislocation emission (AIDE) theory describes the nucleation of dislocations at surfaces that have adsorbed hydrogen, combined with the weakening of atomic bonds. The theory also takes the nucleation and crack growth steps into account [7].
Plenty of variables influence the material behavior towards hydrogen. Also, a combination of the described theories can occur and lead to embrittlement of the material [7, 13].

2.1.3 Prevention of Hydrogen Embrittlement

Different techniques are known to prevent or slow down HE. All the methods are based on the principle that they slow down the diffusion rate or prevent the diffusion into the steel at all.
One option is to use a *low hydrogen annealing* step at 200 °C to reduce the concentration of hydrogen before using the material, but that only prevents the material from pre-existing hydrogen and not from hydrogen uptake during service, for example, in gas pipelines [4, 14, 15].
To prevent the material from HE during service, especially using steel pipelines for hydrogen transportation, it is possible to add a small amount, around 1 %, of other passivating gaseous elements to the hydrogen, but this leads to an extra purification step before using the hydrogen gas [16, 17]. The usable gases also have drawbacks: oxygen in combination with hydrogen leads to an explosive mixture. Carbon monoxide and chlorotrifluoroethylene are toxic; sulfur dioxide and carbon monoxide react

with water to acidic solutions. The mentioned drawbacks and chemical compounds are only a selection [18].
Coatings can also prevent hydrogen diffusion into the steel [13, 19]. One option is to coat the material with a µm-range thick *black oxide* (Fe_3O_4) layer [19, 20]. Also, Ni, Cd, Al or Al−Ni complex films can protect the material by reducing the accessibility for hydrogen [13]. Hard coatings like TiC, Al_2O_3, TiO_2 or Si_3N_4 can be used as a diffusion barrier for hydrogen as the diffusion coefficient is at least seven orders of magnitude lower than for ferrite [19]. Figure 2.3 shows the temperature dependency of the diffusion coefficients of the mentioned coatings as well as for the iron substrate.

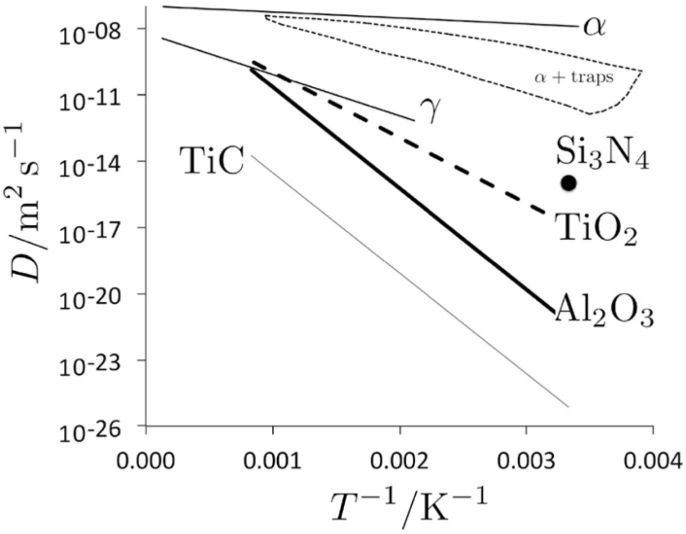

Figure 2.3: Diffusion coefficient over temperature for several hard coatings and γ- and α-iron. The area of the diffusion coefficient of α-iron containing traps is also shown. Reproduced from [19] © 2016 The Iron and Steel Institute of Japan.

Besides using a hard coating, the steel surface can be modified by nitriding or shot peening, both decreases the susceptibility for HE [13]. Nitriding stabilizes the austenitic phase at the surface, leading to a decrease in hydrogen diffusion into the material, especially if the surface layer is thicker than the diffusion length of hydrogen into the material [21]. Shot peening induces some compressive stress, reducing the hydrogen diffusivity into the material. The dislocation density near the surface is also increased. Dislocations are one possible option to trap hydrogen inside of the material. Before the hydrogen can diffuse into the core of the steel, the dislocations are filled with hydrogen. So, the effective diffusion into the core is slowed down, resulting in a higher resistance against HE [13, 22].
Besides the already mentioned dislocations, other structural elements in the material can trap the hydrogen, and the immobilization reduces the risk of damaging the material [23]. The strength of the trap depends on the energy level of it. Figure 2.4 shows the matrix diffusion energy E_{diff}, the trap activation energy E_{t}, the binding energy E_{b} and the detrappping energy E_{d} [24]. The notations of the energies are intermixed between different publications, so it is important to know what was measured [13, 25].

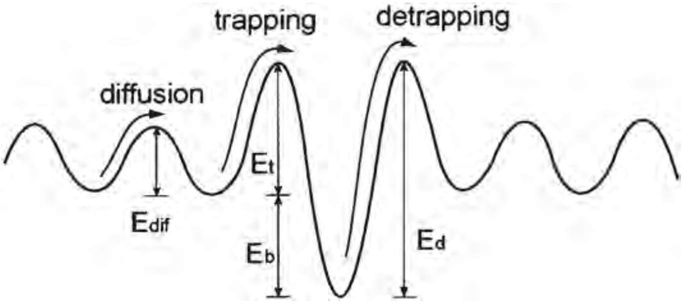

Figure 2.4: Schematic of the diffusion and trapping energy levels inside of trap containing matrix. Reproduced from [24], with permission from Springer Nature.

Depending on the strength of the trap, they can be classified as reversible or irreversible. Examples of reversible traps are interstitial sites, dislocations, grain boundaries, and coherent precipitates. Incoherent precipitates, on the other hand, are considered as irreversible traps [13].

It seems like in carbon steels, the predominant trapping sites are dislocations, but also GBs can trap hydrogen [26–28]. By adding carbide-forming metals, like Ti or V, the resistivity against HE increases because the potential misfit at the surface between the carbide and the matrix acts also as an additional hydrogen trap [26]. Besides the surface of the carbide, internal carbon vacancies can also act as hydrogen traps. For some carbides the activation energy for entering the carbide core is too high to trap hydrogen inside the carbides at ambient temperature [26, 29]. To increase the trapping capability of TiC against hydrogen, Mo can be added to the steel as an additional alloying element. Mo decreases the activation energy for entering the carbide and creates some additional carbon vacancies inside of it [17]. Besides the already mentioned carbides, also, niobium- or chromium carbides can trap hydrogen [26, 30].

A high-resolution microscopy technique is required to analyze the carbides in terms of composition and localization inside the steel, as well as the localization of the trapped hydrogen (deuterium). That high chemical and lateral resolution is provident by the APT [31].

2.2 Atom Probe Tomography

The atom probe tomography is a microscopy technique based on the *field evaporation* of atoms from a surface. The instrument is based on the 1951 from Müller invented field ion microscope (FIM). A positively charged emitter ionizes an imaging gas, the ions are then accelerated to an screen and form there a magnified image of the emitter-tip [32]. By cooling the FIM, in the year 1955, the world's first image with atomic resolution was produced [33]. In 1967, the first prototype of an atom probe (AP) was built by Mülller, Panitz and McLane [34, 35].

2.2.1 Working Principle

To overcome the energy barrier for the field evaporation process, a high electrostatic field E is required. As Equation 2.3 shows, a combination of specimens having a small apex radius R <100 nm combined with a high voltage V is needed. The field factor k is a constant, taking into account the deviation from a spherical surface as well as the electrostatic environment of the specimen. Sharp tips fulfill the requirements and are used as specimens [36, 37].

$$E = \frac{V}{kR}. \tag{2.3}$$

The analysis chamber of the AP is a ultra high vacuum (UHV)-chamber at a pressure $<10^{-10}$ Torr. The remaining gas inside of the analysis chamber is mainly hydrogen. In order to differentiate between the trapped hydrogen from the specimen and the field evaporated hydrogen that originates from the residual gas within the UHV-chamber, the specimens are loaded with deuterium instead of hydrogen [30, 38]. To reduce the thermal vibration of the atom to increase the spatial resolution, reduce unwanted evaporation processes and increasing the vacuum level the specimen is cooled with an He-cryostat [39]. Figure 2.5 shows a schematic structure of the AP.

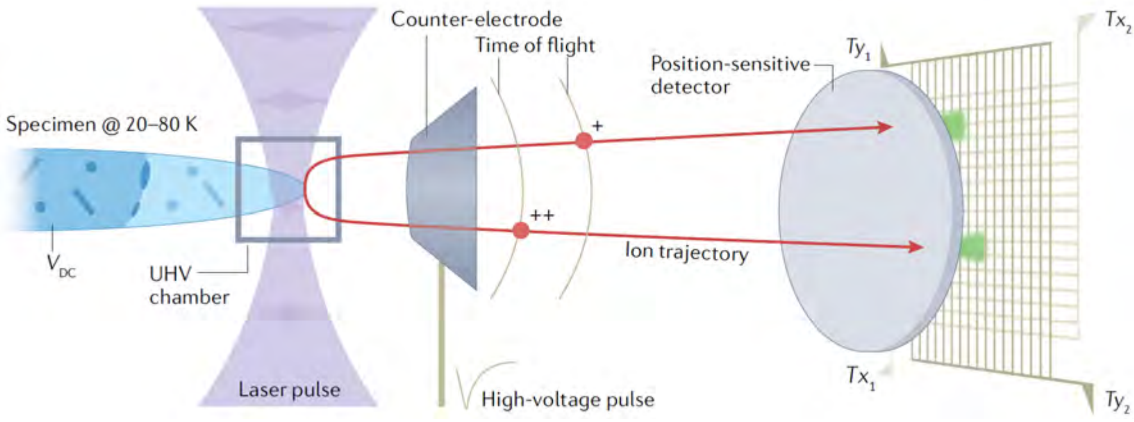

Figure 2.5: Schematic structure of the AP inside of the UHV-chamber. Reproduced from [40], with permission from Springer Nature.

Figure 2.5 indicates already the two possible working modes. The specimen is subjected to a positive base voltage V_{DC}. The field evaporation is then introduced with negative voltage pules V_{p} at the counter-electrode or a laser pulse focused on the specimen tip. The ionized atoms are desorbed and repelled from the surface and flying through the ring shaped counter electrode in the direction of the detector. The trajectory is drawn as a red line [36, 37]. In this thesis only the *voltage mode* is used, so the following description is based on that. The advantage of the *laser mode* is the reduced mechanical stress to the specimen [41]. The drawback of the *laser mode* is the appearance of hydrogen peaks at 1 Da, 2 Da and 3 Da (H^+, ${H_2}^+$, ${H_3}^+$), so the 2 Da hydrogen peak would overlap with the deuterium peak [42, 43]. Additional computational analysis is required to deconvolute the peak, which is essential for determining the accurate concentration of deuterium within the specimen.

The evaporated ions first hit a microchannel plate in a chevron configuration to get secondary electrons and a signal amplification. A crossed delay line detector system measures the impact position on the detector. To increase the measurement accuracy, if multiple ions hit the detector simultaneously, a third delay line at 45° can be added or three are used in a 60° arrangement [37, 44].

The voltage pulse starts a time measurement to determine the chemical identity of the evaporated ion and the impact position on the detector. The electrons generated in the microchannel plate induce an electrical signal inside the wires of the delay line detector. From the measured times the impact positions (X_D, Y_D) can be calculated according to:

$$X_\mathrm{D} = L_x \frac{Tx_2 - Tx_1}{2Tp_\mathrm{x}}, \tag{2.4}$$

where L_x is the length of the detector wire and Tp_x is the total propagation time of an electronic signal through the wire system [37]. The calculation for Y_D is done in the same way.

Some geometrical considerations need to be made to calculate the position of the ion from the detector position. Figure 2.6 shows the trajectory of an evaporate ion. The apex radius of the tip is indicated as R, θ is the real crystallographic and θ' is the observed angle on the detector screen. The image compression factor (ICF) ξ describes the compression between the real and observed angel and can be calculated for small angels in the following way:

$$\xi = \frac{\theta_\mathrm{crystal}}{\theta_\mathrm{observed}} \text{ [37] } . \tag{2.5}$$

The magnification M is defined as:

$$M = \frac{D}{d}\text{[37]}. \tag{2.6}$$

The original position x_tip of the ion is calculated according to:

$$\begin{aligned} x_\mathrm{tip} &= \frac{X_\mathrm{D}}{M} \text{ [37]} \\ &= X_\mathrm{D} \frac{R \sin\left(\xi\theta_\mathrm{observed}\right)}{\sqrt{X_\mathrm{D}^2 + Y_\mathrm{D}^2}}. \end{aligned} \tag{2.7}$$

The calculation for Y_D is done in the same way.

The z coordinate of the ion is calculated based on the assumption that the atoms are evaporated layer-by-layer. The z value is continuously increased, so after one layer is evaporated, the change in z corresponds to one atomic volume [37].

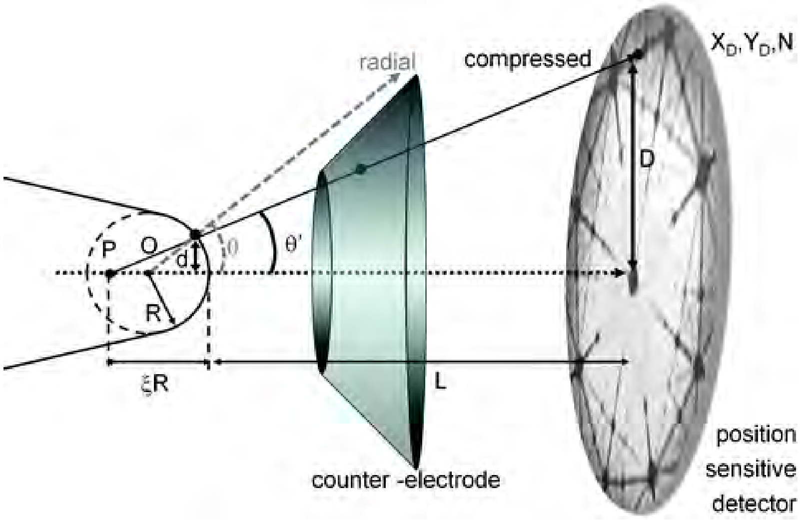

Figure 2.6: Trajectory of an evaporated ion based on the point-projection model. Reproduced from [37], with permission from Springer Nature.

The chemical identity can be determined by equating the potential and kinetic energy before and after the evaporation process, shown in Equation 2.8, where n is the charge of the ion, e is the elementary charge, U is the desorption voltage ($U_{\mathrm{DC}} + U_{\mathrm{p}}$), m is the mass of the ion and v its velocity [34, 37].

$$neU = \frac{1}{2}mv^2. \tag{2.8}$$

Additionally, the time of flight of the ion is required, which is calculated using the following formula:

$$t = \frac{Tx_1 + Tx_2 + Ty_1 + Ty_2}{4} \text{ [44].} \tag{2.9}$$

By rearranging Equation 2.8 and replacing the velocity by the time of flight t and the distance between sample and detector (flight length) L, the mass-to-charge ratio M can be calculated according to:

$$M = \frac{m}{n} = 2eU\left(\frac{t}{L}\right)^2 \tag{2.10}$$

For the reconstruction, the time of flight and the voltage are corrected, so the used algorithm is slightly different, but it is based on the described formulas [39].

2.3 High-Strength Low-Alloy Steel

One option to increase the strength of steels is to use additional (micro)alloying elements like B, Cr, Cu, Mn, Mo, Nb, Si, Ti and V. Some of these elements form precipitates during thermomechanical treatments. The precipitates or the dispersed elements in the matrix hinder the movement of dislocations or GBs. Additionally, the grain growth is suppressed [45, 46]. If the yield strength reaches a minimum of 560 MPa in combination with the before mentioned microalloying, the steel is classified as a HSLA steel [45]. High-strength steels are quite susceptible for HE [7]. But the carbides of the additional (micro)elements can act as traps for the hydrogen and so increase the resistance against HE.

In the orthorhombic cementite (Fe_3C), the surface area plays a key role in trapping hydrogen. The trapping capability is directly proportional to the surface area [47, 48]. The NaCl-type vanadium carbide, which likely occurs as V_4C_3 in steels, has an ordered C-vacancy in its structure. In additon to this structure, a lower C-vacancy structure exists where one sixth of the C lattice sites is unoccupied (V_6C_5). These C-vacancies can act as trapping sites and also reduce the activation energy to trap hydrogen [29, 49]. Titanium carbide exhibits a broad composition range, represented as TiC_{1-x}, where $0 \leq x \leq 0.66$. This carbide has also a rock salt structure but no ordered C-vacancies [50]. The surface coherency is the primary factor determining the trapping capability. For lager incoherent precipitates its unlikely to trap hydrogen via cathodic charging at room temperature (RT). However as motioned in 2.1.3, Mo can decrease the trap activation energy [17, 51].

3

Experimental

3.1 Material

In the thesis, three different HSLA steels are investigated. The composition of the first steel (called in the thesis Steel-1) can be seen in Table 3.1. The steel is investigated in the quenched state: austenitized, hot rolled and water quenched , as well as in a lab-aged state at 600 °C for 4 h. The material was already investigated in a previous publication from Thuvander et al. [46].

Table 3.1: Chemical composition in wt.% of steel-1. Fe in balance [46].

C	Si	Mn	Cr	Mo	V
0.16	0.3	1.3	0.15	0.4	0.04

The second and third steel are studied as received. The second steel contains Fe, C, Si, Mn, Mo, Al, Nb and V. The steel is called in the thesis V-steel. The third steel contains additionally Ti, it is called Ti-steel in the thesis.

3.2 Specimen Preparation

As described in Section 2.2.1, tip-shaped specimens are needed for an APT measurement.

Preparation starts with mechanical cutting and grinding, followed by a sequential two-step electropolishing process. A low-speed saw with a rotating diamond blade is used to cut 500 µm thick plates with dimensions of 15 mm to 20 mm length and 5 mm to 10 mm width from the bulk steel sample. The plates are mechanically thinned down to ∼300 µm by SiC grinding paper and cut with the low-speed saw into 300 µm × 300 µm squared cross section and 15 mm to 20 mm long rods. The deburred rods are clamped into an aluminum handle.

The first step of the electropolishing is done with a thin layer of 10 % perchloric acid in 20 % glycerol and 70 % ethanol floating on Galden®. The experimental setup is shown in Figure 3.1a. A voltage of 18 V is used to etch a broad neck into the rod. The immersion depth must be changed during polishing to get the desired shape. Before the sample breaks into two pieces, the process is stopped. The sample and the electrode are cleaned with ethanol.

The second polishing step uses 2 % perchloric acid in 2-butoxyethanol. A voltage of 18 V is applied with a self-interrupting power supply. The experimental setup is shown in Figure 3.1b. The power supply monitors the current and stops it after the sample breaks. After the breakage, the specimen and the counter-electrode are cleaned with ethanol. The second part of the rod can be used as another APT specimen and is rinsed in ethanol and clamped into an aluminum handle.
A pulse generator, using 18 V, is used for final polishing. The 2 % perchloric acid in 2-butoxyethanol is again used as the electrolyte. The immersion depth must be between the tip's front and the aluminum cylinder. A sequence of 5, 3, 2 and 1 ms pulse-length with three pulses each is used for the polishing. The specimen is cleaned with ethanol and dried in flowing nitrogen gas.

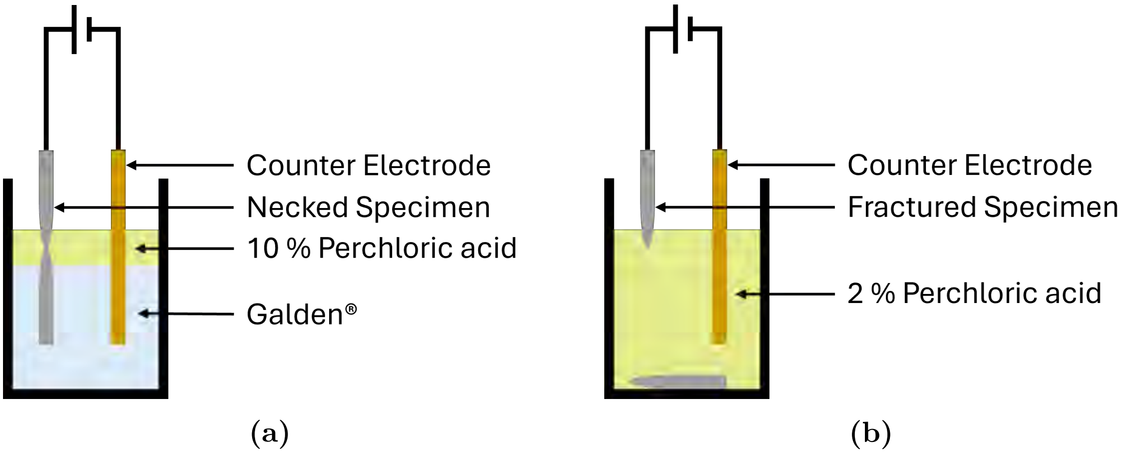

Figure 3.1: Experimental setup for the two electrochemical polishing steps for preparing the AP samples: (a) to create a broad neck on the sample, and (b) for etching the sample until fracture. Based on [37].

3.3 Electrochemical Deuterium Loading

Deuterium is used for electrochemical loading to differentiate it from the residual hydrogen present in the UHV analysis chamber of the AP [30, 38]. For the loading, a 0.1 M NaOH solution in heavy water (D_2O) is used. A voltage of -2.2 V is applied for 30 s or 180 s. The polarity is changed compared to the preparation steps as the minus sign indicates. The experimental setup is shown in Figure 3.2. After loading, the specimen is cleaned with ethanol and dried in a nitrogen flow. The loaded specimens are transferred trough the load-lock and the buffer chamber to the cryogenically cooled stage in the analysis chamber within $\sim$15 min.

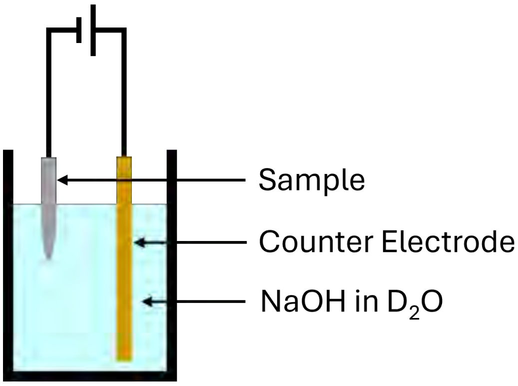

Figure 3.2: Experimental setup for the electrochemical loading with deuterium of the AP samples.

3.4 Atom Probe Measurement and Reconstruction

3.4.1 Acquisition Parameters

The LEAP® 6000 XR from CAMECA Instruments is used in this study. The measurements are done in *voltage mode*. If nothing else is mentioned, the following parameters are used in the experiment.

Table 3.2: Standard parameters for the APT measurement.

Parameter	Value
Temperature T	70 K
Detection rate (DR)	0.3 %
Pulse fraction (PF)	20 %
Pulse rate (PR)	200 kHz

3.4.2 Room Temperature Degassing

To give a more qualitative statement about the strength of the hydrogen traps, a RT degassing experiment is carried out. Specimens from the V- and Ti-steel are loaded with deuterium and measured. The measurement is stopped after a couple of million atoms. The specimen is transferred back to the buffer chamber and stored there at RT followed by measuring the specimen again. That approach is done for the same specimen with two storing periods of 2 h and 4 h.

3.4.3 Calibration of Reconstruction Parameters

The software AP Suite version 6.3.1.110 from CAMECA is used for the reconstruction. The shape of the reconstruction is determined by the ICF and k-factor. Both parameters can be calibrated if the crystallography of the sample is known and visible on the *detector hit map*.
To find the correct ICF ξ, a stereographic projection of ferrite is laid over the visible crystallographic poles on the *detector hit map*. To produce the *hit map*, the MATLAB code from Breen et al. is used. The stereographic projection is created by the WinWULFF software version 1.6.0 from Weber [52, 53]. Figure 3.3 shows an image of the overlaid *hit map*. Due to distortions at the edges, the computed stereographic projection does not completely match the visible poles on the *detector hit map*.

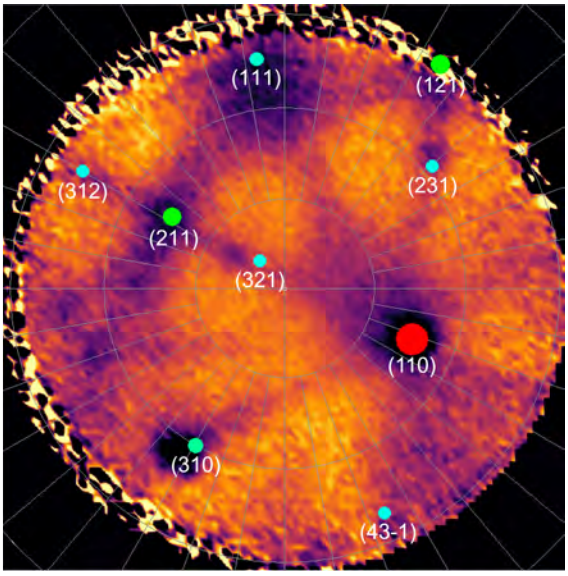

Figure 3.3: Overlaid *detector hit map* with the calculated stereographic projection of ferrite.

To find a proper k-factor, a spatial distribution map of iron at one pole position is plotted. The theoretical spacing of the atoms at a pole is known. By adjusting the value of k, the spacing is tuned to fit the theoretical value. Figure 3.4 shows an image of the ordered iron atoms as well as the spatial distribution map in the z-direction after tuning the k-factor. The images are produced at a (110)-pole. The theoretical spacing for an α-iron (110)-pole is 0.202 nm.

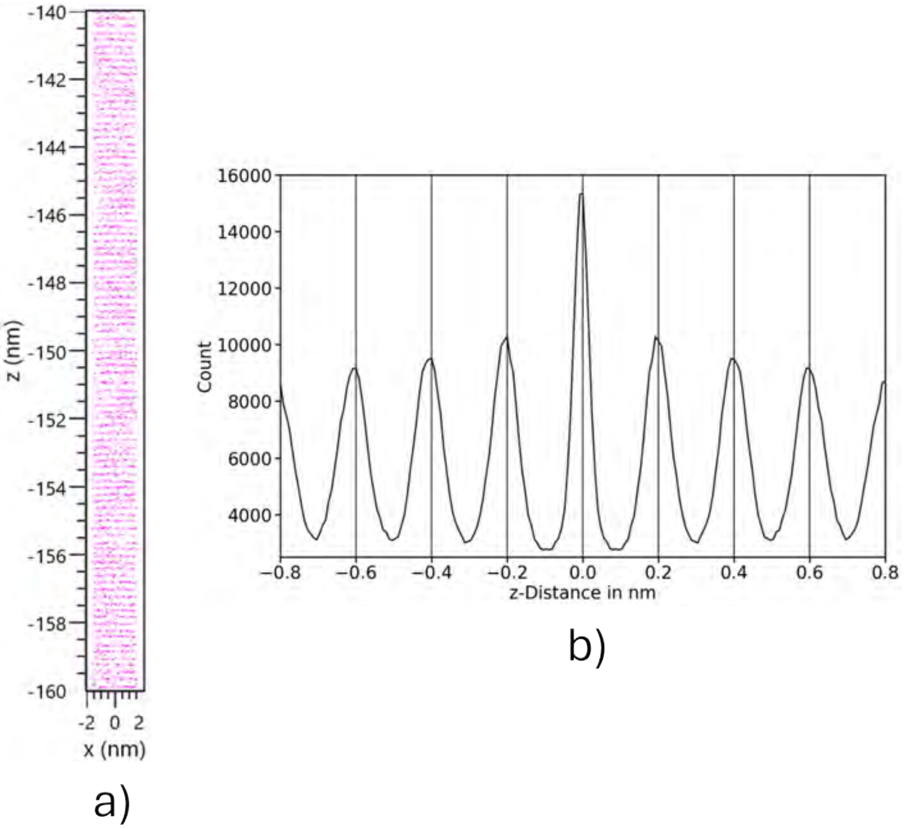

Figure 3.4: Ordered iron structure (a) and the corresponding spatial distribution map (b) after tuning the k-factor at an α-iron (110)-pole. The ICF is determined to be 1.53 and the k-factor is determined to be 4.7.

4

Results and Discussion

Reference measurements in the unloaded state were conducted for all three materials. The datasets corresponding to these reference measurements are not included in this thesis. To illustrate the difference between a specimen in the unloaded and loaded state, Figure 4.1 provides an example of a background corrected mass spectrum, for a Ti-Steel specimen in both the unloaded and D loaded state. An additional peak at 2 Da, corresponding to D^+, is evident in the loaded specimen depicted in Figure 4.1b.

In the reconstructions only a fraction of the total measured iron atoms are shown, with the objective of visualizing the shape of the specimen. All *proxigrams* are generated with a bin width of 0.1 nm.

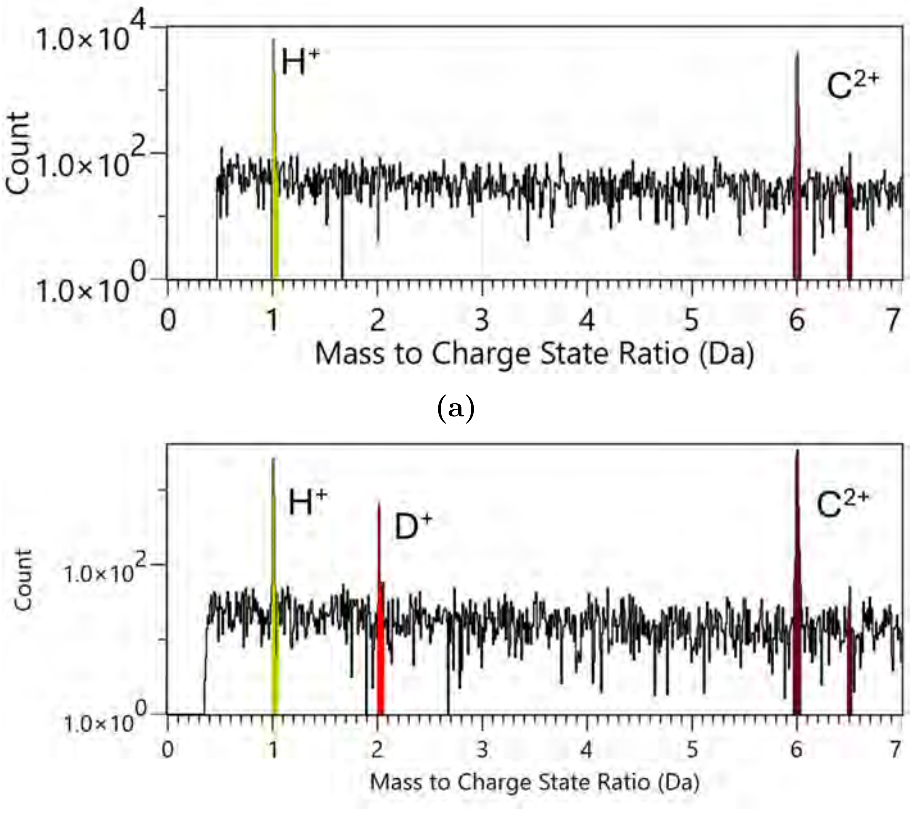

(a)

(b)

Figure 4.1: Illustration of the background corrected mass spectra of Ti-steel specimens up to 7 Da, comparing the unloaded state (a) and the D loaded state (b).

4.1 Steel-1

The Steel-1 is investigated in the quenched (Section 4.1.1) and heat treated (Section 4.1.2) state.

4.1.1 Steel-1 Quenched

Two measurements were carried out for the quenched Steel-1. The shown results are based on a measurement with ∼23 million detected ions. Figure 4.2 shows the background corrected mass spectrum up to 7 Da. The mass spectrum already indicates that the loading was unsuccessful, as no 2 Da peak from the deuterium is visible.

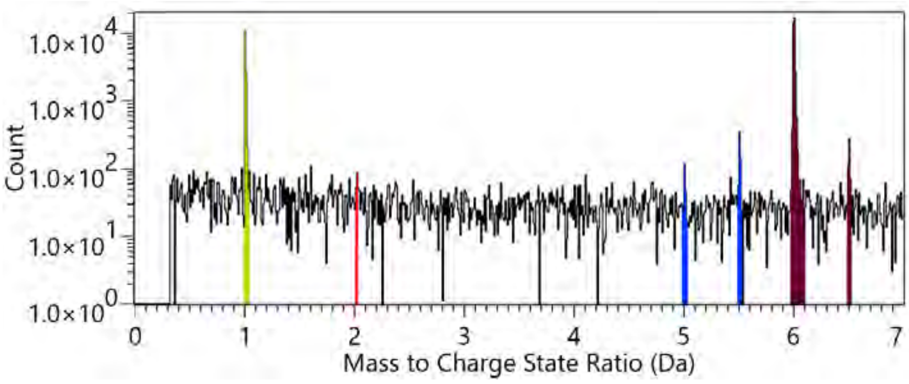

Figure 4.2: Background corrected mass spectrum of a quenched specimen of Steel-1 up to 7 Da.

The complete mass spectrum from the measurement is shown in the Appendix Figure A.1. A second measurement can be found in Appendix Figure A.2 to A.5 confirming the results. The second measurement was done with different conditions: the loading time was increased from 30 s to 180 s and the PR was decreased from 200 kHz to 125 kHz.

Figure 4.3 shows the reconstructed first measurement. Figure 4.3a shows the iron atoms in pink and the two different kinds of carbides inside the specimen. The two carbides are shown as isosurfaces, one with a combined concentration of (C, Mo, V) >3.4 at.%, depicted in orange. The second has a concentration of C >8.0 at.%, shown in dark red. Figure 4.3b and Figure 4.3c show the measured carbon atoms, the two arrows beside each image indicate a GB inside the specimen. Three *detector hit maps* are shown in Figure 4.4 to confirm the presence of different grains.

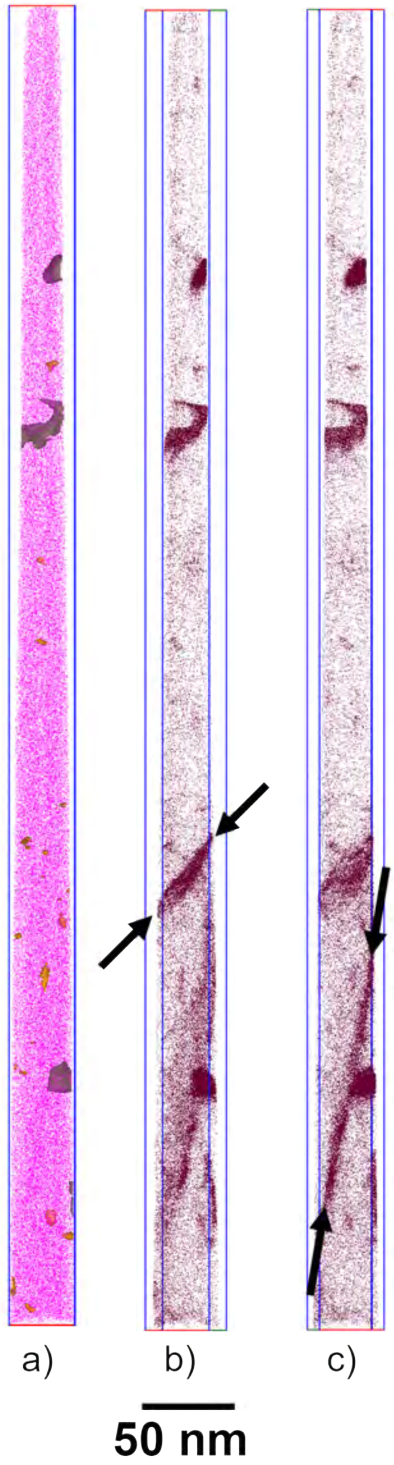

Figure 4.3: Overview of a quenched Steel-1 specimen. Showing in a) the measured Fe atoms in pink. The isosurfaces with a combined concentration of (C, Mo, V) >3.4 at.% are shown in orange. The isosurfaces with a concentration of C >8.0 at.% are shown in dark red. b) and c) are rotated views of the measured C atoms with arrows indicating the GBs

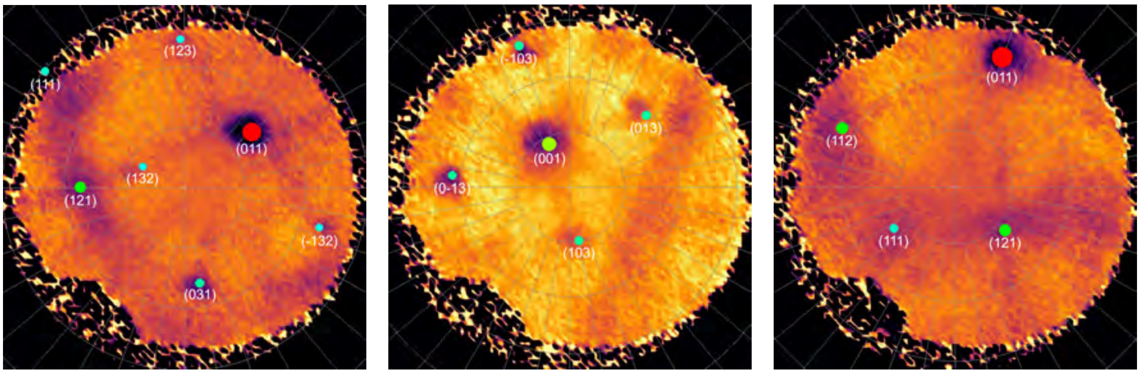

(a) **(b)** **(c)**

Figure 4.4: Three indexed *Detector hit maps* of different depths to indicate the presence of different grains inside a quenched specimen of Steel-1: (a) first grain, (b) second grain, and (c) third grain.

The possible H traps inside the specimen are discussed in more detail to prove that the loading was unsuccessful.

The specimen has two types of traps: the carbides and the GBs. To investigate the trapping capability of the carbides, a *proxigram* of each isosurface type is created. Only the concentrations of C and D are shown for the carbides, as the other alloying elements showed no difference in concentration between the matrix and the carbide. Figure 4.5 shows the *proxigram* of the isosurfaces with a C concentration >8.0 at.%. It is visible that the C concentration increases continuously with increasing depth. When the carbide core is reached, the curve flattens out, with the maximum concentration reaching ~25 at.%. Based on the C concentration, the carbide can be identified as cementite (Fe_3C). Based on the data, D trapping does not seem to occur.

Figure 4.6 shows the *proxigram* of the isosurface with a combined concentration of (C, Mo, V) >3.4 at.%. For that carbide, no matching chemical formula can be found. It is visible that the C concentration continuously increases while going deeper into the carbide. It reaches a maximum of 9 at.% in a depth of 1.3 nm. Based on the data, D trapping does not seem to occur.

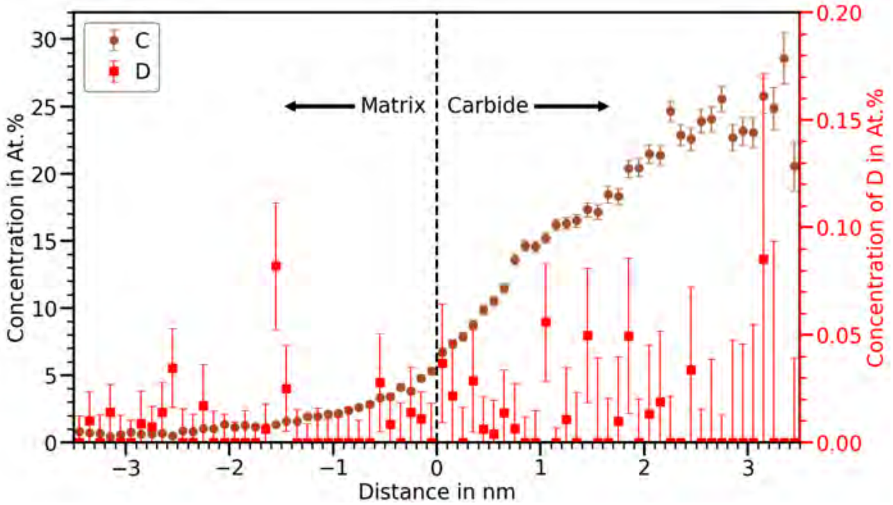

Figure 4.5: *Proxigram* of the isosurfaces with a C concentration >8.0 at.%, showing the concentration of C and D as a function of the distance to the isosurface of a quenched Steel-1 specimen.

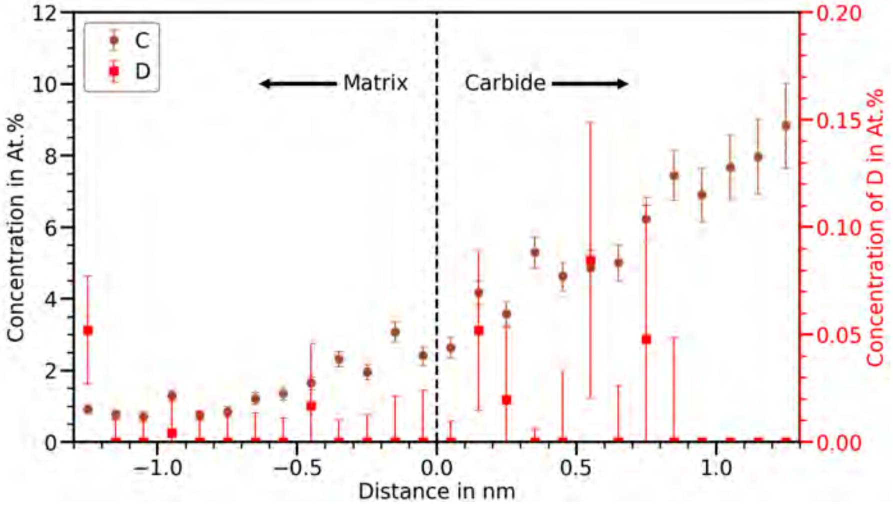

Figure 4.6: *Proxigram* of the isosurfaces with a combined concentration of (C, Mo, V) >3.4 at.%, showing the concentration of C and D as a function of the distance to the isosurface of a quenched Steel-1 specimen.

A cylinder is positioned through each GB to characterize their trapping capability. The cylinder, through the first GB, has a length of 12.5 nm, with semi-axis lengths of 25.7 nm and 26.7 nm. The cylinder, through the second GB, has a length of 26.6 nm, with semi-axis lengths of 25.2 nm and 39.0 nm. 1D-concentration profiles with a bin width of 0.2 nm are generated with the atoms inside the cylinder. Figure 4.7 shows the *1D-concentration profile* of C and D of the first GB and Figure 4.8 of the second one. The other elements are not shown because no segregation was visible. In terms of the trapping capability, both GBs show the same behavior, of trapping no D. The C concentration is with 3 at.% for the second GB only half as high as for the first GB. Generating an isosurface specific to the GB could not be achieved, as no element or combination of elements would produce a smooth surface.

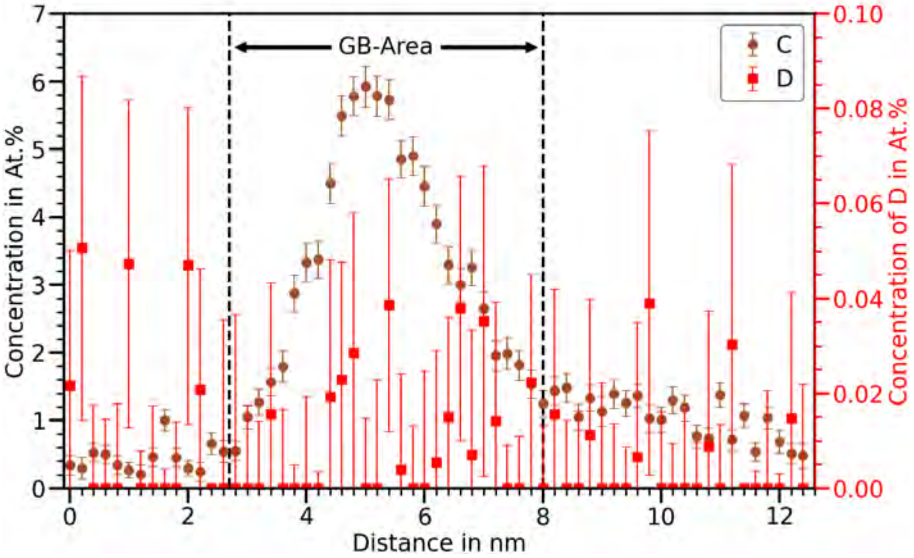

Figure 4.7: *1D-concentration profile* of a cylinder trough the first GB in a quenched Steel-1 specimen, showing the concentration of C and D as a function of the distance.

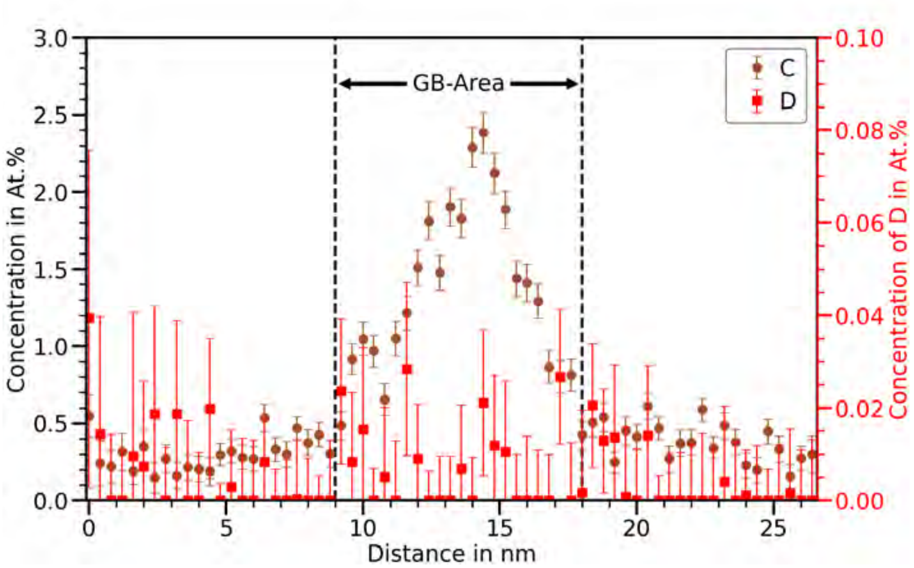

Figure 4.8: *1D-concentration profile* of a cylinder trough the second GB in a quenched Steel-1 specimen, showing the concentration of C and D as a function of the distance.

As the evaluation shows, the D loading was unsuccessful. However, the *proxigrams/1D-concentration profiles* are created with the 2 Da events to ensure that the D was not trapped by the carbides or the GBs. Since there is no visible concentration increase, the *proxigrams/1D-concentration profiles* only show the measurement background. To investigate the weak traps, the specimens need to be immediately cooled to cryogenic temperatures after loading and transferred under cryogenic conditions into the AP [54].

4.1.2 Steel-1 Heat treated

To increase the size of the carbides, the quenched Steel-1 was heat treated at 600 °C for 4 h. In total, four successful measurements of the loaded material were carried out. In the thesis, one data set is discussed in more detail and one is added in the Appendix to confirm the results; Figure A.7 to A.10.
The discussed data set comprises ~20.1 million detected ions, with the PR set to 125 kHz. For the data shown in the Appendix, the loading time was increased from 30 s to 180 s. The measurement was conducted at a PR of 125 kHz as well. The complete mass spectrum of the measurement can be seen in the Appendix Figure A.6. Figure 4.9 shows the background corrected mass spectrum up to 7 Da. In hand with the mass spectrum, deuterium should be present in the specimen. Figure 4.10 shows the Fe atoms in pink and the isosurfaces of the two different types of carbides inside the specimen. In orange, a combined concentration surface of (C, Mo, V) >3.4 at.% and in dark red, a concentration surface C >8.0 at.% is shown.

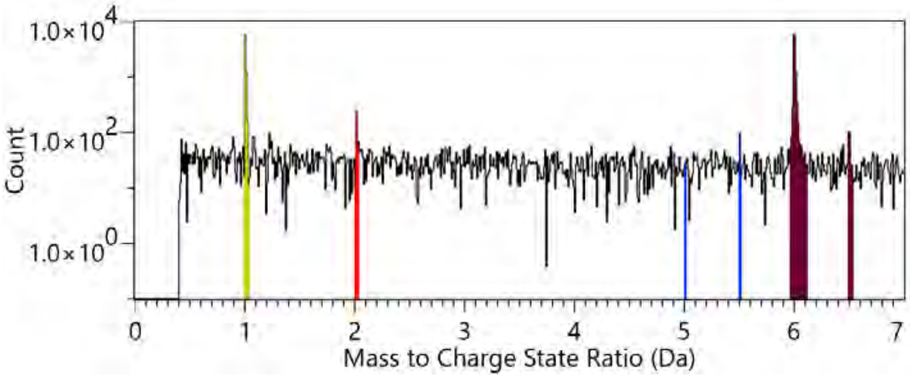

Figure 4.9: Background corrected mass spectrum of a heat treated Steel-1 specimen up to 7 Da.

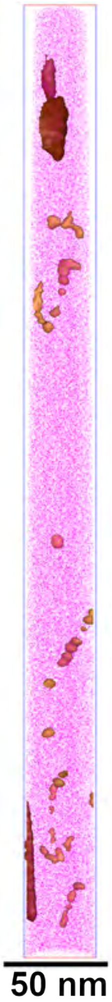

Figure 4.10: Overview of a heat treated Steel-1 specimen, showing the measured Fe atoms in pink. The isosurfaces with a combined concentration of (C, Mo, V) >3.4 at.% are shown in orange. The isosurfaces with a concentration of C >8.0 at.% are shown in dark red.

To investigate the hydrogen trapping capability of the carbides, *proxigrams* for each type of carbide are generated. Figure 4.11 shows the *proxigrams* of the isosurface with a C concentration >8.0 at.%. The C concentration increases while going deeper into the carbide and flattens in the core of the carbide. The concentration reaches a value of ~25 at.%. Based on the maximum concentration in the carbide core, it is identified as cementite. The other alloying elements enrich inside the carbide, except for Si. Remarkable is the enrichment of Mn from 12 at.% to 16 at.% in the core. The *proxigram* analysis reveals that there is no observable increase in the concentration of D within the carbide. This suggests that trapping of hydrogen does not occur.

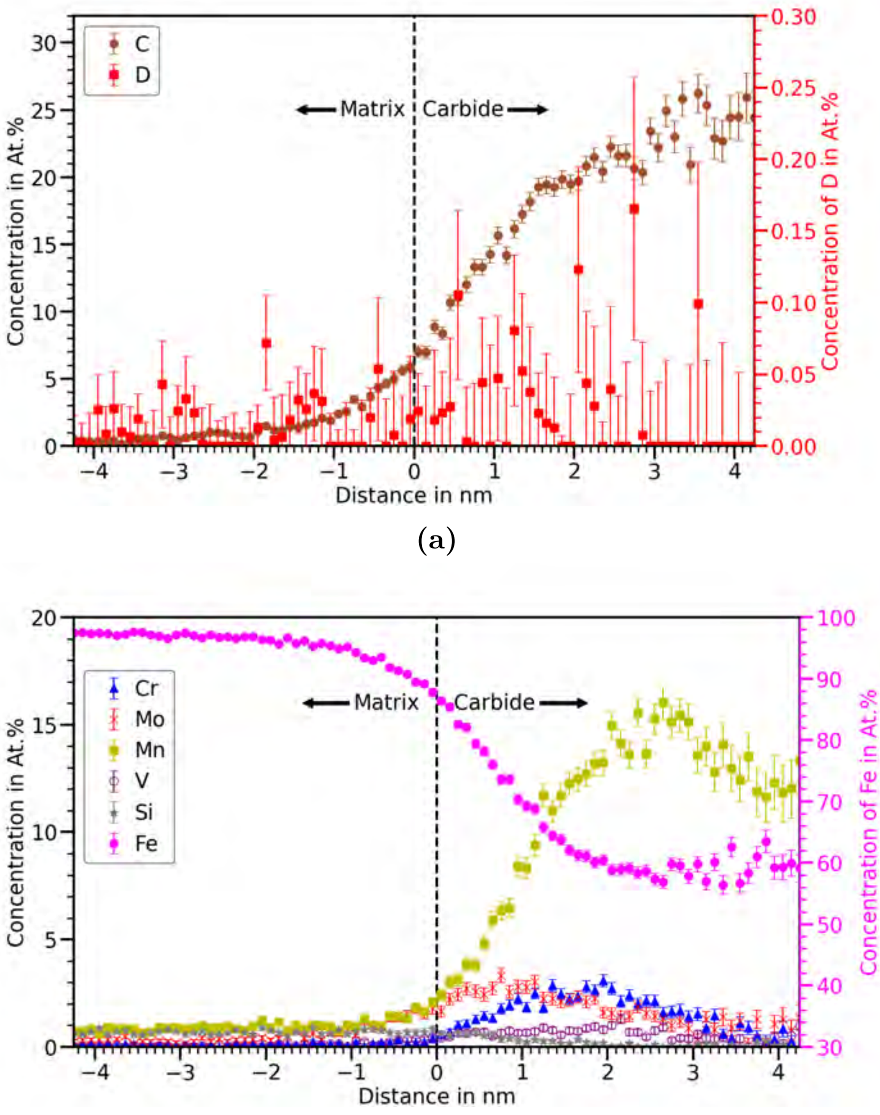

(a)

(b)

Figure 4.11: *Proxigrams* of the isosurfaces with a concentration of C >8.0 at.%, showing the concentration as a function of the distance to the isosurface of a heat treated Steel-1 specimen: (a) concentration of C and D, and (b) concentration of Cr, Mo, Mn, V, Si, and Fe.

In Figure 4.12, the *proxigrams* of the isosurfaces with a combined concentration (C, Mo, V) >3.4 at.% are shown. The C concentration increases while going deeper into the carbide. The other alloying elements enrich inside the carbide, except for Si. The trapping capability of the carbide can be argued as the data points for 1.25 nm to 1.45 nm are not zero but the error bar reaches zero for the first two points. For the last point the minimum concentration reaches 0.05 at.% which is close to the matrix concentration. However the mass spectrum shows a 2 Da peak, indicating some D is inside of the specimen. It may be possible that the carbides act as weak traps and hence slow down diffusion through the matrix.

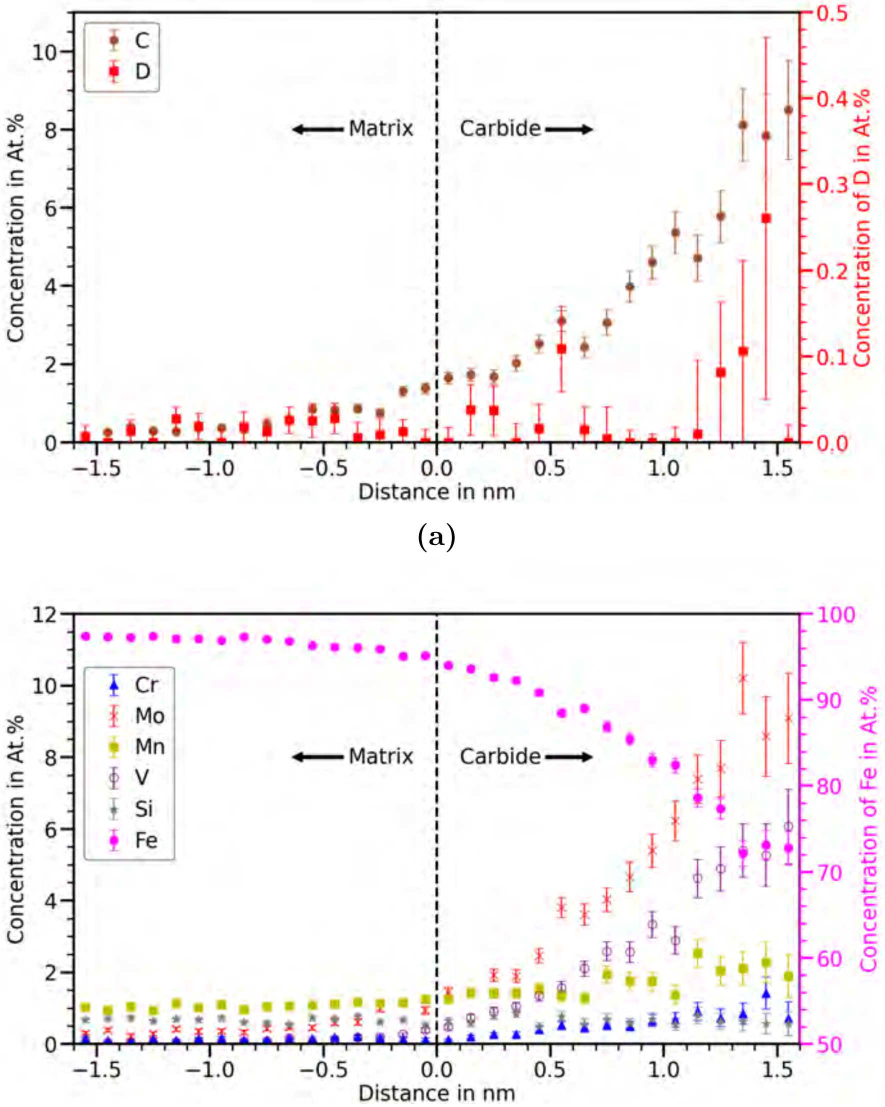

(a)

(b)

Figure 4.12: *Proxigrams* of the isosurfaces with a combined concentration of (C, Mo, V) >3.4 at.%, showing the concentration as a function of the distance to the isosurface of a heat treated Steel-1 specimen: (a) concentration of C and D, and (b) concentration of Cr, Mo, Mn, V, Si, and Fe.

4.2 V-Steel

In total, three successful measurements of loaded specimens were carried out. In the thesis, one data set is discussed in more detail and one is added in the Appendix to confirm the results; Figure A.13 to A.16.
The discussed data set comprises ∼3.3 million detected ions and was obtained with a DR of 0.5 %. The complete mass spectrum of the measurement can be found in the Appendix Figure A.12. Figure 4.13 shows the background corrected mass spectrum of a V-steel specimen up to 7 Da. A significant 2 Da peak from D^+ is visible.

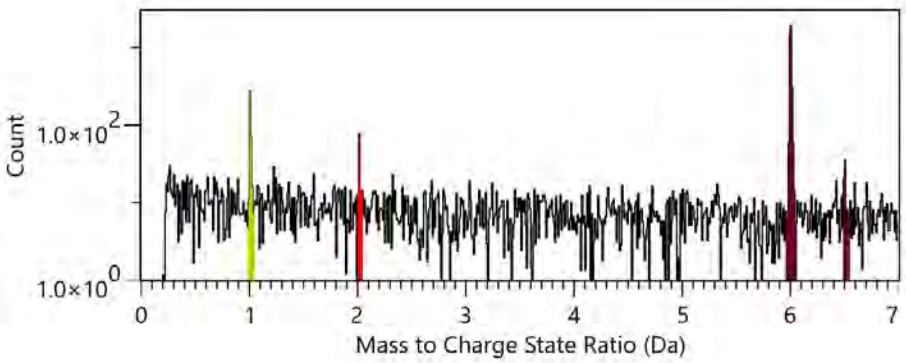

Figure 4.13: Background corrected mass spectrum of a V-steel specimen up to 7 Da.

Figure 4.14 shows the reconstructed specimen, in a) the Fe atoms in pink and the isosurfaces with a combined concentration of (C, Mo, V) >3.4 at.% are shown. The arrows indicate the “big” precipitates. The others are characterized as “small” ones. In b), the measured V and D are shown, c) and d) are showing 10 nm thick slices in higher magnification to visualize the trapping sites of the carbides.

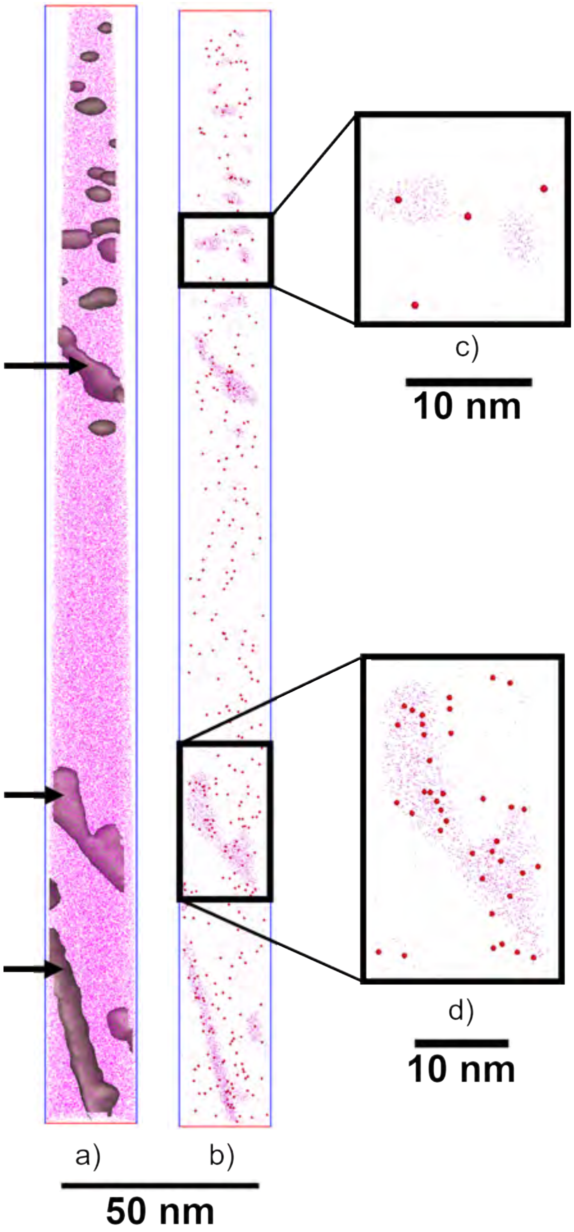

Figure 4.14: Overview of the V-steel sample. Showing in a) the measured Fe atoms in pink. The isosurfaces of a combined concentration of (C, Mo, V) >3.4 at.% are shown in brown. In b), the V (pink) and D (red) atoms of the measurement are shown. c) and d) show details from 10 nm thick slices.

The magnified parts from the specimen and the mass spectrum indicated that trapping occurs inside the "big" carbides. To investigate the trapping capability of the carbides in more detail, *proxigrams* of the "big" and "small" carbides were created, shown in Figure 4.15 and 4.16.
Based on the V to C ratio for the "big" carbides in the core, the carbide is identified as V_4C_3, which is the more likely carbide modification in steels [29]. The V and C concentration increases while going deeper into the carbide. The maximum value differs between the two size classes, but the values are similar when looking at the same distances from the isosurface. The same applies for the D concentration.

No D is detected in the core region of the larger precipitates. This is consistent with other publications. They claim that additional C vacancies are more likely between the surface and the core, and those C vacancies act as the trapping sites for the D [29, 49, 55]. In contrast to that, Chen et al. measured that D also gets trapped inside the core of the carbide, without additional D trapping on/near the surface [56]. For the in the Appendix shown measurement (Figure A.16a), it looks like the trapping also takes place in the core of the carbides but the length scale is different, 2.0 nm compared with 2.5 nm. The peak value is reached at 2 nm for the in Figure 4.15a shown measurement, so both measurements show the same behavior. The other alloying elements have an increased concentration inside the carbide, except for Si.

Based on the calculations from Ivanchenko et al., it is clear that the measured Fe concentration inside the carbide is way too high, as the solubility of Fe in the carbide is quite low [57]. The increased iron concentration observed within the carbide is a consequence of a measurement artifact known as *local magnification*. This is due to the higher evaporation field of the carbide in comparison to the matrix. The carbides are depicted larger in the reconstruction, reflecting not their actual size. The result is an overlap between matrix and carbide. This effect is less pronounced for larger precipitates, as the carbide covers a larger surface area, and the evaporation field becomes more equal [37, 39, 44, 58] .

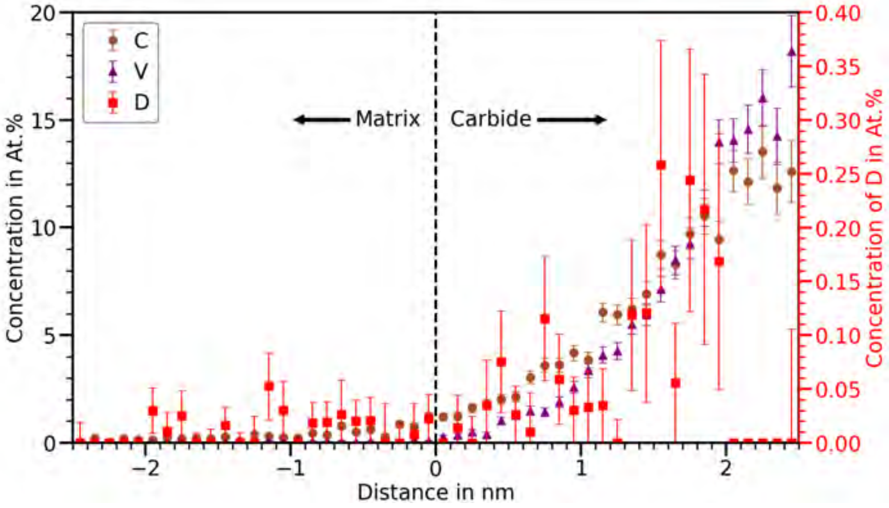

(a)

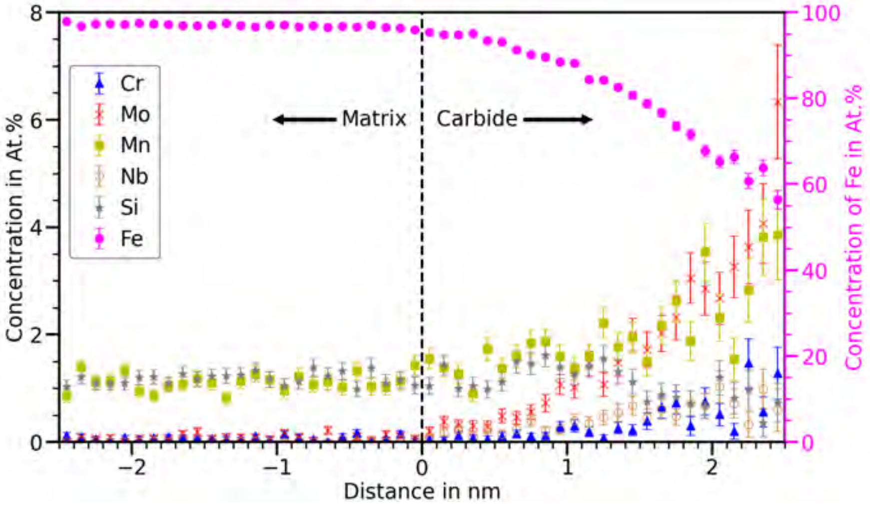

(b)

Figure 4.15: *Proxigrams* of the isosurfaces for the “big” carbides with a combined concentration of (C, Mo, V) >3.4 at.%, showing the concentration as a function of the distance to the isosurface of a V-steel specimen: (a) concentration of C, V, and D, and (b) concentration of Cr, Mo, Mn, Nb, Si, and Fe.

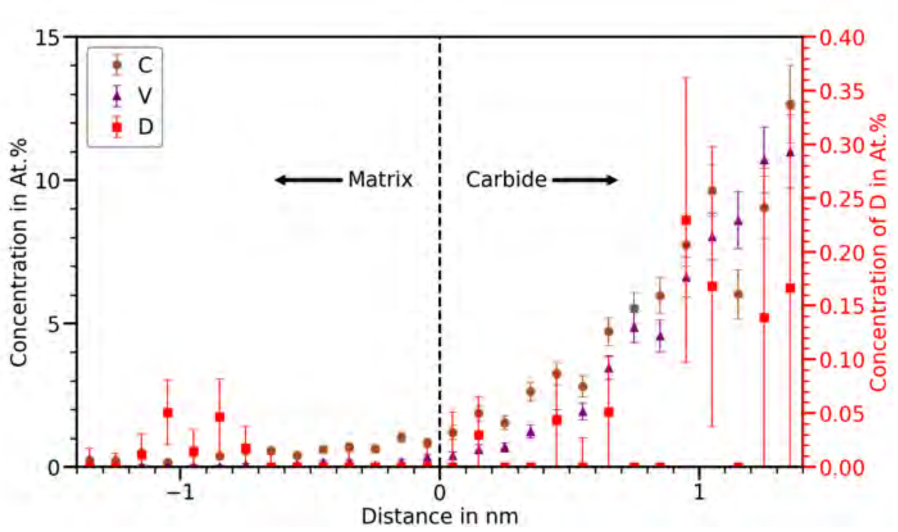

(a)

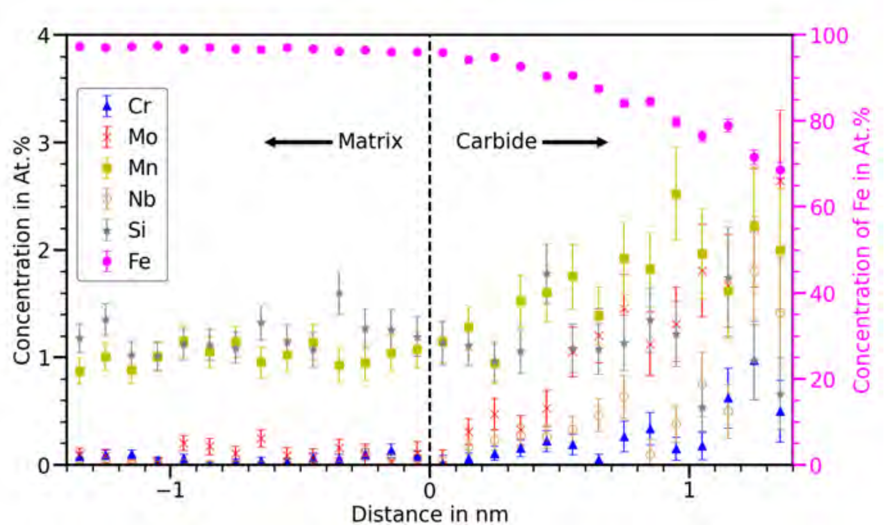

(b)

Figure 4.16: *Proxigrams* of the isosurfaces for the “small” carbides with a combined concentration of (C, Mo, V) >3.4 at.%, showing the concentration as a function of the distance to the isosurface of a V-steel specimen: (a) concentration of C, V, and D, and (b) concentration of Cr, Mo, Mn, Nb, Si, and Fe.

4.3 Ti-Steel

In total, three successful measurements of the loaded material were carried out. In the thesis, one data set is discussed in more detail and one is added in the Appendix to confirm the results;Figure A.18 to A.21.
The discussed data set comprises ∼11.2 million detected ions. The complete mass spectrum of the measurement can be found in the Appendix Figure A.17. Figure 4.17 shows the background corrected mass spectrum of a Ti-steel specimen up to 7 Da.

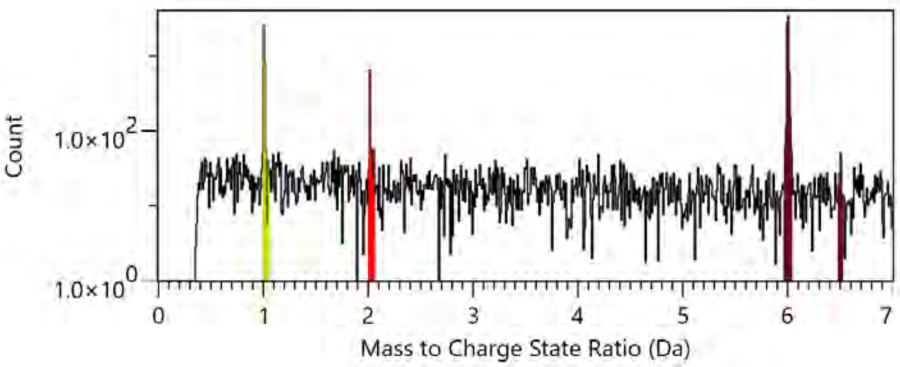

Figure 4.17: Background corrected mass spectrum of a Ti-steel specimen up to 7 Da.

Figure 4.18 shows the reconstructed specimen, in a) the Fe atoms and the isosurfaces with the concentration of Ti >2.0 at.% are shown. In b), the measured Ti and D atoms are visualized, and c) shows a 10 nm slice in higher magnification.

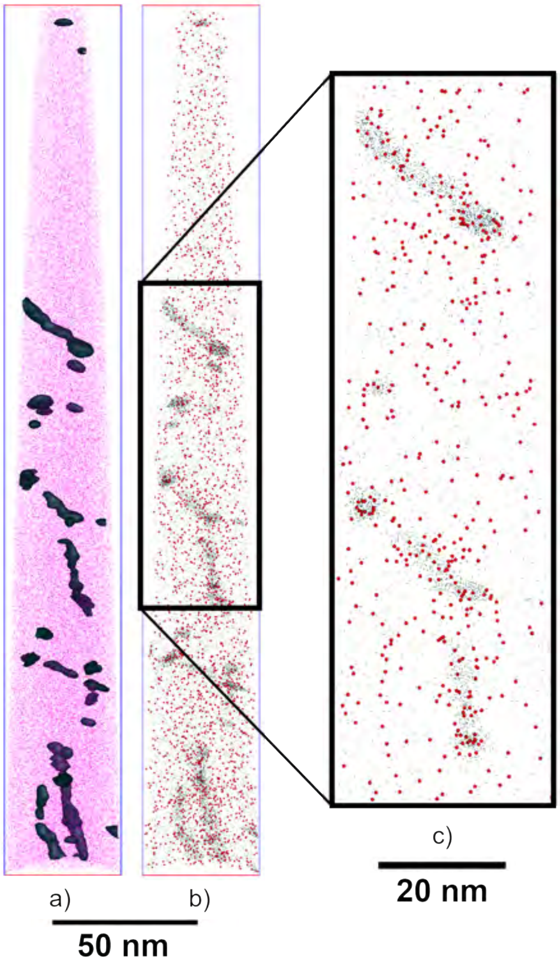

Figure 4.18: Overview of a Ti-steel specimen. Showing in a) the measured Fe atoms in pink. The isosurfaces with a Ti-concentration >2.0 at.% are shown in dark green. In b), the Ti (dark green) and D (red) atoms are visualized. In c) a 10 nm thick slice is shown.

The magnified part and the mass spectrum indicate that trapping takes place. To have a more detailed view, a *proxigram* of the carbides is generated, shown in Figure 4.19. The C and Ti concentration increases while going deeper into the carbide and reaches ∼20 at.% in the core of the carbide. The D concentration also increases with the depth, reaching a value of ∼1 at.%. Except for Si, the concentration of the other alloying elements increases inside of the carbides.

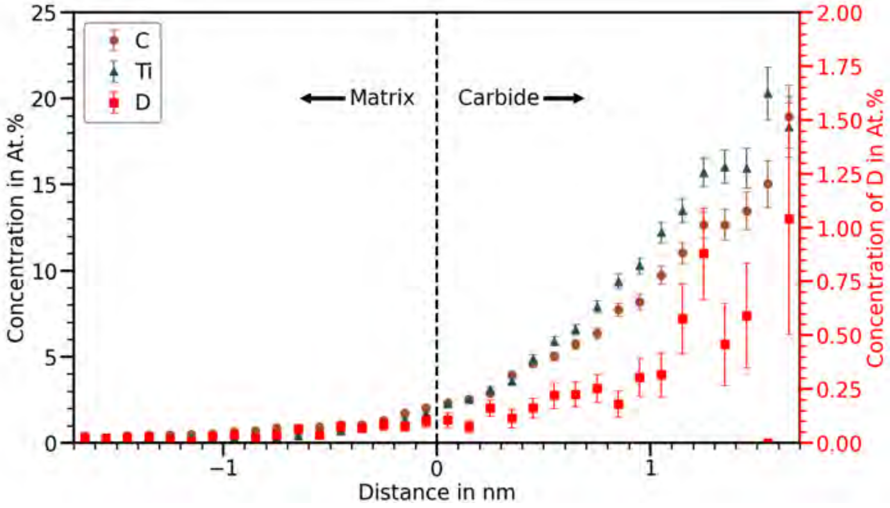

(a)

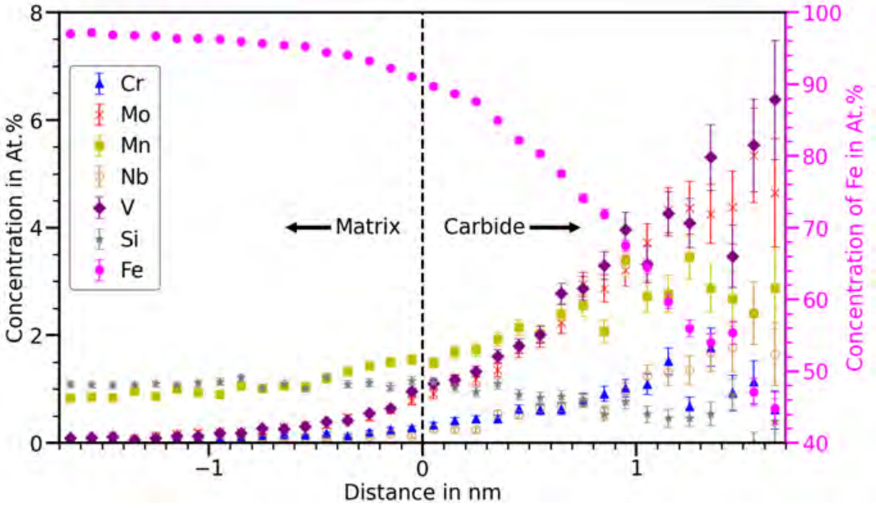

(b)

Figure 4.19: *Proxigrams* of the isosurfaces with a concentration of Ti >2.0 at.%, showing the concentration as a function of the distance to the isosurface of a Ti-steel specimen: (a) concentration of C, Ti, and D, and (b) concentration of Cr, Mo, Mn, Nb, V, Si, and Fe.

The carbides are characterized as titanium carbides. According to Lebrun et al., the high Fe concentration inside the carbide can be classified as a measurement artifact [59]. One reason for the high Fe content is the in Section 4.2 already described *local magnification*. Beside this effect a *peak overlap* of Ti and C occurs; meaning the ions have the same/a similar *time of flight*. The *peak overlap* is exemplary explained for the 24 Da region in Table 4.1 and visualized in Figure 4.20. The peaks can be decomposed via the natural abundance of the isotopes. The *peak decomposition* is an optimization including some errors but the error of not decompose the peaks is way lager.

The primary carbide ions hit the detector in the same area and nearly simultaneously. The detector requires a specific time interval between two events to detect both events if they are present in the same position or within a short time frame. If the second ion arrives at the detector within that time window, the second ion can't be detected [37, 39]. For Ti carbides both effects (peak overlap and detector dead time) occur, so the probability of not detecting all evaporated ions increases. An indication of missing atoms is the too low 24 Da peak, see Figure 4.20. The 24 Da peak should be higher than the expected abundance for ^{48}Ti as the peak also contains ^{12}C. This problem is also discussed in other publications, so the measurement is in hand with the already known problem [17, 60].

Table 4.1: Illustration of the peak overlap between Ti and C in the 24 Da-peak region.

Mass to Charge ratio in Da	Ti^{2+} occurs	C_2^+ occurs	C_4^{2+} occurs
23	✓		
23.5	✓		
24	✓	✓	✓
24.5	✓		✓
25	✓	✓	✓

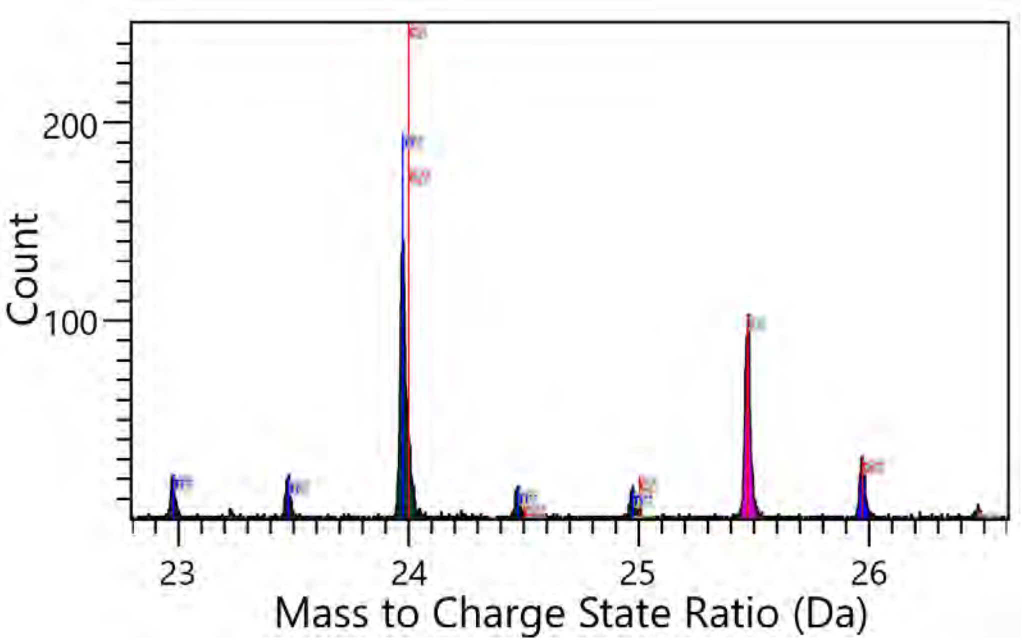

Figure 4.20: Section of the mass spectrum of a Ti-steel specimen to illustrate the peak overlap between Ti and C in that region. The abundance of Ti is leveled with the peaks $^{46}Ti^{2+}$ and $^{47}Ti^{2+}$. The abundance for C_2^+ and C_4^{2+} are not leveled and are shown to see the overlap. Besides Ti and C also V and Cr are shown with leveled abundance. At 23.25 Da a Nb-peak is visible but not indicated in the image.

TiC exists in a wide composition range, so it is expected that the Ti to C ratio is not 1:1 [50]. Besides the wide range, $2\,\mathrm{Mo}^{2+}$- can substitute $2\,\mathrm{Ti}^{4+}$-ions in the crystal structure. To maintain charge neutrality one C vacancies need to be created, lowering the C content further [17]. The *Kröger-Vink notation* for that exchange is shown in Reaction 4.1.

$$2\,\mathrm{Ti_{Ti}}^{\times} + \mathrm{C_C}^{\times} + 2\,\mathrm{Mo_S}^{2+} \longrightarrow 2\,\mathrm{Mo_{Ti}}'' + \mathrm{V_C}^{\bullet\bullet\bullet\bullet} + 2\,\mathrm{Ti_S}^{4+} + \mathrm{C_S}^{4-} \tag{4.1}$$

The carbon vacancies can act as additional trapping sites for the D, and the Mo atoms also decrease the energy barrier for the indiffusion of D to the carbide core [17].

4.4 Room Temperature Degassing

To get a qualitative insight into the strength of the traps, a *room temperature degassing* experiment was carried out. Following an initial measurement, the V- and Ti-steel specimens were stored in the buffer chamber of the AP at RT for 2 h, then measured again. This was followed by a further 4 h storage and subsequent measurement under identical conditions. This means that, for the same specimen, data points were generated at 0.25 h, 2.25 h, and 6.25 h. To characterize the trapping strength, the D concentration inside of the carbides is plotted over the storing time (Figure 4.21a). The decrease of the D concentration with increasing degassing time is clearly visible. The D concentration is at least three times as high in the Ti-steel than in the V-steel. Figure 4.21b shows the relative D concentration normalized to the starting concentration of the specimen. The relative decrease for the V-steel is way higher than for the Ti-steel. Combining the data from Figure 4.21a and Figure 4.21b it is clearly visible, that the titanium carbide is the better D trap in terms of absolute amount and trapping strength.

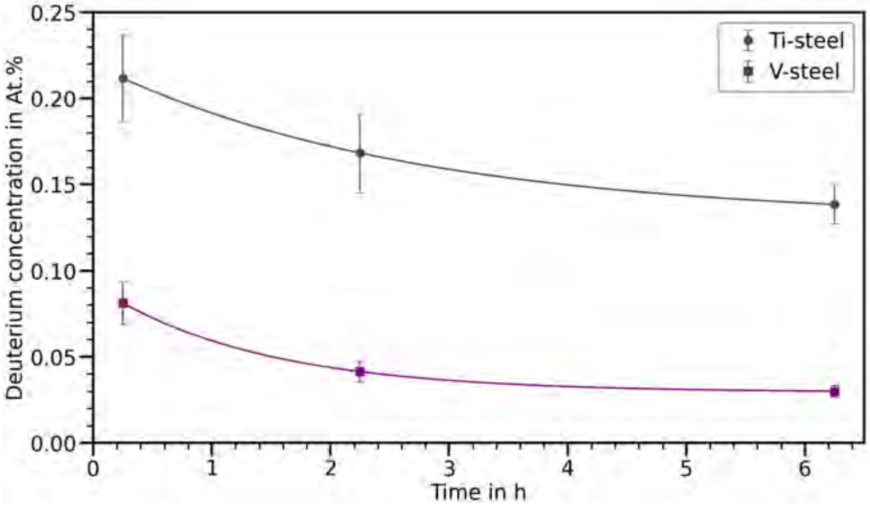

(a)

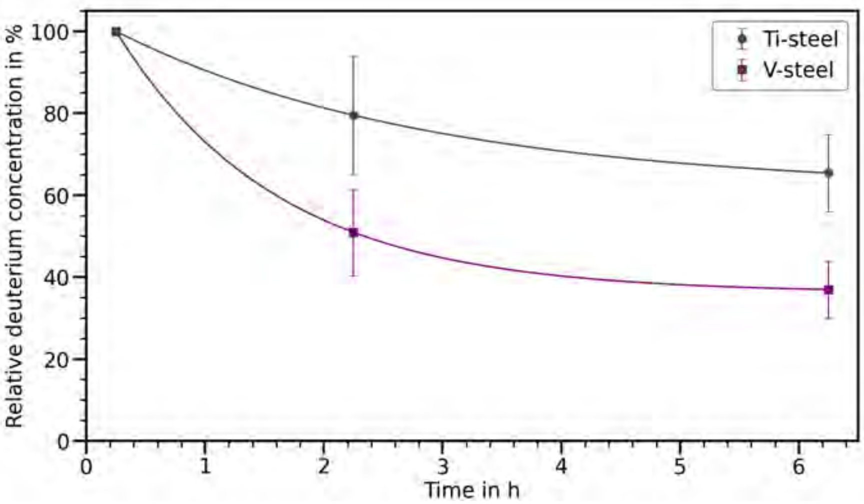

(b)

Figure 4.21: Comparison of the D concentration inside the carbides of the V- and Ti-steel during a RT degassing experiment: (a) after different storing times at RT and (b) the relative D concentration of the V- and Ti-steel normalized to the starting concentration of the specimen.

4.5 Comparison

For the Steel-1, no trapping can be seen in the quenched state. The larger carbides from the heat-treated specimens may trap D but definitely reduce the effective diffusion constant of the material. Also, the composition of the carbides differs between the quenched and heat-treated material. The increase of the concentration of additional alloying elements in the carbides for the heat treated material can increase the trapping capability by introducing more vacancies or increase generally the D affinity.

Ti and V carbides exhibit stronger trapping capabilities compared to cementite and the second carbide in Steel-1. Both Ti- and V-Steel demonstrate D trapping. In V-Steel, the D concentration reaches approximately ∼0.25 at.%, whereas in Ti-Steel, the concentration exceeds 1 at.%. Consequently, the amount of trapped D is higher in Ti-Steel than in V-Steel. A similar trend is observed in the degassing experiment, where the initial concentration within the isosurface volumes is approximately ∼0.2 at.% for Ti-steel and only ∼0.08 at.% for V-steel. Furthermore, the relative decrease observed during the degassing experiment indicates a higher trapping strength for Ti-steel. This finding is consistent with other publications, which characterize Ti carbides as stronger traps compared to V carbides [19, 26].

5

Summary and Conclusion

The aim of the thesis was to investigate the trapping capability of different types of carbides in different low alloyed steels using APT.
The specimens for the APT measurement were prepared by a two-step electropolishing process in perchloric acid. For the electrochemical D loading process a voltage of $-2.2\,\mathrm{V}$ was applied and a $0.1\,\mathrm{M}$ NaOH in heavy water solution was used as an electrolyte. The specimens were transferred within ~15 min to the analysis chamber of the AP where the specimen is cooled to cryogenic temperatures.
The APT measurements were carried out with the LEAP® 6000 XR from CAMECA Instruments. For the evaluation the software AP Suite version 6.3.1.110 from CAMECA was used. For all measurements a crystallographic calibration was carried out, to find proper values for the ICF and k-factor.
For the quenched Steel-1 no trapping can be seen. The carbide size and the concentration of the additional alloy elements inside of the carbides are increased in the annealed sample, which is a potential reason for the higher D concentration in the material. Therefore, the effective diffusion coefficient for the annealed material is probably lower than for the quenched one.
The Ti- and V-steel show D trapping, which was evident from the mass spectra and the *proxigrams*. Beside the normal measurements also a *room temperature degassing* experiment was carried out for the Ti- and V-steel. The specimens are stored in the *buffer chamber* for different time periods, to get qualitative insight into the strength of the traps. Ti carbide is the stronger trap compared to V carbide. Not only does Ti carbides trap more D, but also retain it to a greater extent.

6

Future Work

For further investigations of the trapping strength of the different carbides, a thermal desorption mass spectrometry (TDMS) measurement can/should be carried out. With the TDMS, the de-trapping energy and the amount of the trapped hydrogen can be measured [30]. In this thesis, the hydrogen at 1 Da was ignored in the evaluation because of the known problem of residual hydrogen in the analysis chamber (see Section 2.2.1). To investigate if the unloaded specimen already has trapped hydrogen inside of the specimen, a measurement series of low hydrogen annealed specimens in the *load lock* of the AP can be carried out while comparing the amount of measured hydrogen at 1 Da of the annealed and non annealed specimens. If there is already some pre-trapped hydrogen in the specimens, the 1 Da peak of the low hydrogen annealed specimens is smaller than for the non-annealed specimens. A slow strain rate tensile test of the loaded and nonloaded material can be carried out to investigate the influence of hydrogen on the mechanical properties of the used materials in this thesis.

Bibliography

[1] Sunita Sharma and Sib Krishna Ghoshal. “Hydrogen the future transportation fuel: From production to applications”. In: *Renewable and Sustainable Energy Reviews* 43 (2015), pp. 1151–1158. ISSN: 13640321. DOI: `10.1016/j.rser.2014.11.093`.

[2] *Hydrogen*. URL: `https://energy.ec.europa.eu/topics/energy-systems-integration/hydrogen_en` [Accessed on: May 22, 2024].

[3] Pasquale Marcello Falcone, Michael Hiete, and Alessandro Sapio. “Hydrogen economy and sustainable development goals: Review and policy insights”. In: *Current Opinion in Green and Sustainable Chemistry* 31 (2021), p. 100506. ISSN: 24522236. DOI: `10.1016/j.cogsc.2021.100506`.

[4] Satu Lipiäinen et al. “Use of existing gas infrastructure in European hydrogen economy”. In: *International Journal of Hydrogen Energy* 48.80 (2023), pp. 31317–31329. ISSN: 03603199. DOI: `10.1016/j.ijhydene.2023.04.283`.

[5] Sankara Papavinasam. “Mechanisms”. In: *Corrosion Control in the Oil and Gas Industry*. Elsevier, 2014, pp. 249–300. ISBN: 9780123970220. DOI: `10.1016/B978-0-12-397022-0.00005-4`.

[6] Yun Chung. *Validity of Caltrans’ Environmental Hydrogen Embrittlement Tests on Grade BD Anchor Rods in the SAS Span*. Dec. 2, 2014. URL: `https://trid.trb.org/view/1335242`.

[7] S. P. Lynch. “Hydrogen embrittlement (HE) phenomena and mechanisms”. In: *Stress Corrosion Cracking*. Elsevier, 2011, pp. 90–130. ISBN: 9781845696733. DOI: `10.1533/9780857093769.1.90`.

[8] Mathias Truschner, Anton Trautmann, and Gregor Mori. “The Basics of Hydrogen Uptake in Iron and Steel”. In: *BHM Berg- und Hüttenmännische Monatshefte* 166.9 (2021), pp. 443–449. ISSN: 0005-8912. DOI: `10.1007/s00501-021-01142-x`.

[9] Johannes Rehrl. “Wasserstoffversprödung in hochfesten, mikrolegierten Stählen”. PhD thesis. Technische Universität München, 2014. URL: `https://mediatum.ub.tum.de/1177864`.

[10] D. G. Westlake. “A generalized model for hydrogen embrittlement”. In: *Trans. ASM (Transactions of American Society for Metals)* (1969), pp. 1000–1006.

[11] L. B. Pfeil. “The effect of occluded hydrogen on the tensile strength of iron”. In: *Proceedings of the Royal Society of London. Series A, Containing Papers of a Mathematical and Physical Character* 112.760 (1926), pp. 182–195. ISSN: 0950-1207. DOI: `10.1098/rspa.1926.0103`.

[12] C. D. Beachem. “A new model for hydrogen-assisted cracking (hydrogen “embrittlement”)”. In: *Metallurgical Transactions* 3.2 (1972), pp. 441–455. ISSN: 0026-086X. DOI: `10.1007/BF02642048`.

[13] Xinfeng Li et al. “Review of Hydrogen Embrittlement in Metals: Hydrogen Diffusion, Hydrogen Characterization, Hydrogen Embrittlement Mechanism and Prevention”. In: *Acta Metallurgica Sinica (English Letters)* 33.6 (2020), pp. 759–773. ISSN: 1006-7191. DOI: `10.1007/s40195-020-01039-7`.

[14] Hye-Jin Kim et al. “Baking Effect on Desorption of Diffusible Hydrogen and Hydrogen Embrittlement on Hot-Stamped Boron Martensitic Steel”. In: *Metals* 9.6 (2019), p. 636. DOI: `10.3390/met9060636`.

[15] Chengshuang Zhou et al. “Effects of internal hydrogen and surface-absorbed hydrogen on the hydrogen embrittlement of X80 pipeline steel”. In: *International Journal of Hydrogen Energy* 44.40 (2019), pp. 22547–22558. ISSN: 03603199. DOI: `10.1016/j.ijhydene.2019.04.239`.

[16] Andrej Atrens et al. “Feasibility of the Use of Gas Phase Inhibition of Hydrogen Embrittlement in Gas Transmission Pipelines Carrying Hydrogen: A Review”. In: *JOM* 75.1 (2023), pp. 232–238. ISSN: 1047-4838. DOI: `10.1007/s11837-022-05559-8`.

[17] Pang-Yu Liu et al. “Engineering metal-carbide hydrogen traps in steels”. In: *Nature communications* 15.1 (2024), p. 724. DOI: `10.1038/s41467-024-45017-4`.

[18] J. H. Holbrook et al. “Control of hydrogen embrittlement of metals by chemical inhibitors and coatings”. In: *Gaseous Hydrogen Embrittlement of Materials in Energy Technologies*. Elsevier, 2012, pp. 129–153. ISBN: 9780857095367. DOI: `10.1533/9780857095374.1.129`.

[19] Harshad Kumar Dharamshi Hansraj Bhadeshia. “Prevention of Hydrogen Embrittlement in Steels”. In: *ISIJ International* 56.1 (2016), pp. 24–36. ISSN: 0915-1559. DOI: `10.2355/isijinternational.ISIJINT-2015-430`.

[20] S. W. Ooi, P. Yan, and R. H. Vegter. “Black oxide coating and its effectiveness on prevention of hydrogen uptake”. In: *Materials Science and Technology* 35.1 (2019), pp. 12–25. ISSN: 0267-0836. DOI: `10.1080/02670836.2018.1530425`.

[21] Toshihiro Tsuchiyama et al. “Suppression of hydrogen embrittlement by formation of a stable austenite layer in metastable austenitic stainless steel”. In: *Scripta Materialia* 90-91 (2014), pp. 14–16. ISSN: 13596462. DOI: `10.1016/j.scriptamat.2014.07.005`.

[22] Xin-feng Li et al. “Effect of shot peening on hydrogen embrittlement of high strength steel”. In: *Int J Miner Metall Mater (International Journal of Minerals, Metallurgy and Materials)* 23.6 (2016), pp. 667–675. DOI: `10.1007/s12613-016-1279-z`.

[23] B. A. Szost, R. H. Vegter, and Pedro E. J. Rivera-Díaz-del-Castillo. “Hydrogen-Trapping Mechanisms in Nanostructured Steels”. In: *Metallurgical and Materials Transactions A* 44.10 (2013), pp. 4542–4550. ISSN: 1073-5623. DOI: `10.1007/s11661-013-1795-7`.

[24] F. G. Wei, T. Hara, and K. Tsuzaki. “Precise determination of the activation energy for desorption of hydrogen in two Ti-added steels by a single thermal-

desorption spectrum”. In: *Metallurgical and Materials Transactions B* 35.3 (2004), pp. 587–597. ISSN: 1073-5615. DOI: `10.1007/s11663-004-0057-x`.

[25] Xinfeng Li et al. “Effect of tempering temperature and inclusions on hydrogen-assisted fracture behaviors of a low alloy steel”. In: *Materials Science and Engineering: A* 682 (2017), pp. 359–369. ISSN: 09215093. DOI: `10.1016/j.msea.2016.11.064`.

[26] F. G. Wei and K. Tsuzaki. “Hydrogen trapping phenomena in martensitic steels”. In: *Gaseous Hydrogen Embrittlement of Materials in Energy Technologies*. Elsevier, 2012, pp. 493–525. ISBN: 9781845696771. DOI: `10.1533/9780857093899.3.493`.

[27] C. San Marchi. “Hydrogen embrittlement of stainless steels and their welds”. In: *Gaseous Hydrogen Embrittlement of Materials in Energy Technologies*. Elsevier, 2012, pp. 592–623. ISBN: 9781845696771. DOI: `10.1533/9780857093899.3.592`.

[28] Thorsten Michler and Michael P. Balogh. “Hydrogen environment embrittlement of an ODS RAF steel – Role of irreversible hydrogen trap sites”. In: *International Journal of Hydrogen Energy* 35.18 (2010), pp. 9746–9754. ISSN: 03603199. DOI: `10.1016/j.ijhydene.2010.06.071`.

[29] Jun Takahashi, Kazuto Kawakami, and Yukiko Kobayashi. “Origin of hydrogen trapping site in vanadium carbide precipitation strengthening steel”. In: *Acta Materialia* 153 (2018), pp. 193–204. ISSN: 13596454. DOI: `10.1016/j.actamat.2018.05.003`.

[30] Severin Jakob et al. “Characterization of hydrogen traps in a co-precipitation steel investigated by atom probe experiments without cryogenic transfer”. In: *Scripta Materialia* 243 (2024), p. 115963. ISSN: 13596462. DOI: `10.1016/j.scriptamat.2023.115963`.

[31] M. K. Miller et al. *Atom Probe Field Ion Microscopy*. Oxford University PressOxford, 1996. ISBN: 9780198513872. DOI: `10.1093/oso/9780198513872.001.0001`.

[32] Erwin W. Müller. “Das Feldionenmikroskop”. In: *Z. Physik (Zeitschrift für Physik)* 131.1 (1951), pp. 136–142. DOI: `10.1007/BF01329651`.

[33] Erwin W. Müller. “Resolution of the Atomic Structure of a Metal Surface by the Field Ion Microscope”. In: *Journal of Applied Physics* 27.5 (1956), pp. 474–476. ISSN: 0021-8979. DOI: `10.1063/1.1722406`.

[34] Erwin W. Müller, John A. Panitz, and S. Brooks McLane. “The Atom-Probe Field Ion Microscope”. In: *The Review of scientific instruments* 39.1 (1968), pp. 83–86. ISSN: 0034-6748. DOI: `10.1063/1.1683116`.

[35] M. K. Miller. *Atom Probe Tomography: Analysis at the Atomic Level*. Boston, MA: Springer US, 2000. ISBN: 978-1-4613-6921-9. DOI: `10.1007/978-1-4615-4281-0`.

[36] D. Blavette and X. Sauvage. “Early Developments and Basic Concepts”. In: *Atom Probe Tomography*. Elsevier, 2016, pp. 1–15. ISBN: 9780128046470. DOI: `10.1016/B978-0-12-804647-0.00001-2`.

[37] Baptiste Gault et al. *Atom Probe Microscopy*. Vol. 160. New York, NY: Springer New York, 2012. ISBN: 978-1-4614-3435-1. DOI: `10.1007/978-1-4614-3436-8`.

[38] G. Sundell, M. Thuvander, and H-O Andrén. “Hydrogen analysis in APT: methods to control adsorption and dissociation of H_2”. In: *Ultramicroscopy* 132 (2013), pp. 285–289. DOI: `10.1016/j.ultramic.2013.01.007`.

[39] David J. Larson et al. *Local Electrode Atom Probe Tomography: A User’s Guide*. New York, NY: Springer New York, 2013. ISBN: 978-1-4614-8720-3. DOI: `10.1007/978-1-4614-8721-0`.

[40] Baptiste Gault et al. “Atom probe tomography”. In: *Nature reviews. Methods primers* 1.51 (2021). DOI: `10.1038/s43586-021-00047-w`.

[41] A. Vella and J. Houard. “Laser-Assisted Field Evaporation”. In: *Atom Probe Tomography*. Elsevier, 2016, pp. 251–278. ISBN: 9780128046470. DOI: `10.1016/B978-0-12-804647-0.00008-5`.

[42] R. Prakash Kolli. “Controlling residual hydrogen gas in mass spectra during pulsed laser atom probe tomography”. In: *Advanced structural and chemical imaging* 3.1 (2017), p. 10. ISSN: 2198-0926. DOI: `10.1186/s40679-017-0043-4`.

[43] Yi-Sheng Chen et al. “Atom Probe Tomography for the Observation of Hydrogen in Materials: A Review”. In: *Microscopy and Microanalysis* 29.1 (2023), pp. 1–15. ISSN: 1431-9276. DOI: `10.1093/micmic/ozac005`.

[44] Michael K. Miller and Richard G. Forbes. *Atom-Probe Tomography: The Local Electrode Atom Probe*. Boston, MA: Springer US, 2014. ISBN: 978-1-4899-7429-7. DOI: `10.1007/978-1-4899-7430-3`.

[45] George E. Totten, Lin Xie, and Kiyoshi Funatani. *Handbook of Mechanical Alloy Design*. CRC Press, 2003. ISBN: 9781135522780. DOI: `10.1201/9780203913307`.

[46] Mattias Thuvander, Hans Magnusson, and Ulrika Borggren. “Carbide Precipitation in a Low Alloyed Steel during Aging Studied by Atom Probe Tomography and Thermodynamic Modeling”. In: *Metals* 11.12 (2021), p. 2009. DOI: `10.3390/met11122009`.

[47] Gye-Won Hong and Jai-Young Lee. “The interaction of hydrogen and the cementite-ferrite interface in carbon steel”. In: *Journal of Materials Science* 18.1 (1983), pp. 271–277. ISSN: 0022-2461. DOI: `10.1007/BF00543835`.

[48] H. K. D. H. Bhadeshia. “Cementite”. In: *International Materials Reviews* 65.1 (2020), pp. 1–27. ISSN: 0950-6608. DOI: `10.1080/09506608.2018.1560984`.

[49] Reiner Kirchheim. “Changing the interfacial composition of carbide precipitates in metals and its effect on hydrogen trapping”. In: *Scripta Materialia* 160 (2019), pp. 62–65. ISSN: 13596462. DOI: `10.1016/j.scriptamat.2018.09.043`.

[50] Sigemaro Nagakura and Shiguéo Oketani. “Structure of Transition Metal Carbides”. In: *Transactions of the Iron and Steel Institute of Japan* 8.5 (1968), pp. 265–294. ISSN: 0021-1583. DOI: `10.2355/isijinternational1966.8.265`.

[51] F. G. Wei and K. Tsuzaki. “Quantitative analysis on hydrogen trapping of TiC particles in steel”. In: *Metallurgical and Materials Transactions A* 37.2 (2006), pp. 331–353. ISSN: 1073-5623. DOI: `10.1007/s11661-006-0004-3`.

[52] A. J. Breen et al. “Revealing latent pole and zone line information in atom probe detector maps using crystallographically correlated metrics”. In: *Ultramicroscopy* 243 (2023), p. 113640. DOI: `10.1016/j.ultramic.2022.113640`.

[53] Steffan Weber. *WinWULFF*. 2018. URL: `http://www.jcrystal.com/products/winwulff/` [Accessed on: May 3, 2024].

[54] Yi-Sheng Chen et al. “Observing hydrogen in steel using cryogenic atom probe tomography: A simplified approach”. In: *International Journal of Hydrogen Energy* 44.60 (2019), pp. 32280–32291. ISSN: 03603199. DOI: `10.1016/j.ijhydene.2019.09.232`.

[55] Rofiques Salehin, Gregory B. Thompson, and Christopher R. Weinberger. “Hydrogen trapping and storage in the group IVB-VIB transition metal carbides”. In: *Materials & Design* 214 (2022), p. 110399. ISSN: 02641275. DOI: `10.1016/j.matdes.2022.110399`.

[56] Y-S Chen et al. “Direct observation of individual hydrogen atoms at trapping sites in a ferritic steel”. In: *Science (New York, N.Y.)* 355.6330 (2017), pp. 1196–1199. DOI: `10.1126/science.aal2418`.

[57] Volodymyr Ivanchenko, Tatyana Pryadko, and Materials Science International Team. *C-Fe-V Ternary Phase Diagram Evaluation.* 2007. URL: `https://materials.springer.com/msi/docs/sm_msi_r_10_010103_01` [Accessed on: May 30, 2024].

[58] F. Vurpillot, A. Bostel, and D. Blavette. “Trajectory overlaps and local magnification in three-dimensional atom probe”. In: *Applied Physics Letters* 76.21 (2000), pp. 3127–3129. ISSN: 0003-6951. DOI: `10.1063/1.126545`.

[59] Nathalie Lebrun, Pierre Perrot, and Materials Science International Team. *C-Fe-Ti Ternary Phase Diagram Evaluation.* 2007. URL: `https://materials.springer.com/msi/docs/sm_msi_r_10_013964_01` [Accessed on: May 30, 2024].

[60] M. Thuvander et al. “Quantitative atom probe analysis of carbides”. In: *Ultramicroscopy* 111.6 (2011), pp. 604–608. DOI: `10.1016/j.ultramic.2010.12.024`.

Appendix

A.1 Quenched Steel-1

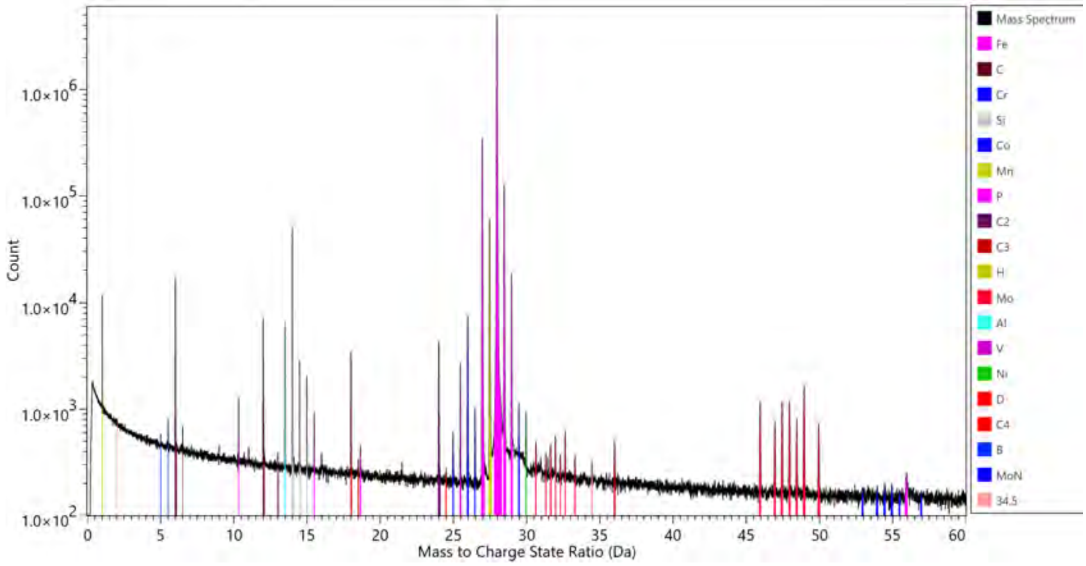

Figure A.1: Indexed mass spectrum of a quenched Steel-1 specimen.

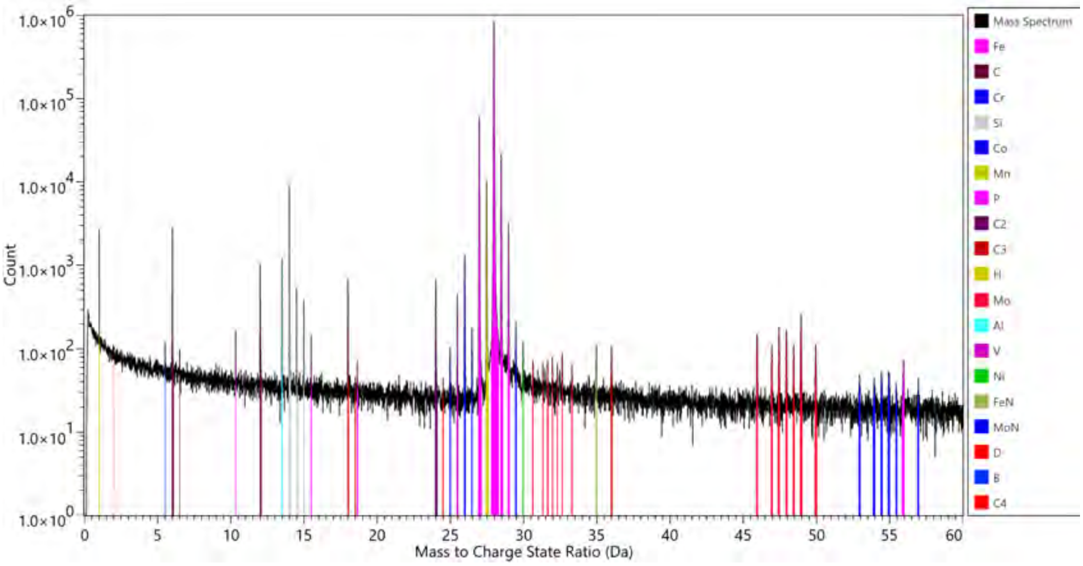

Figure A.2: Indexed mass spectrum of a quenched Steel-1 specimen.

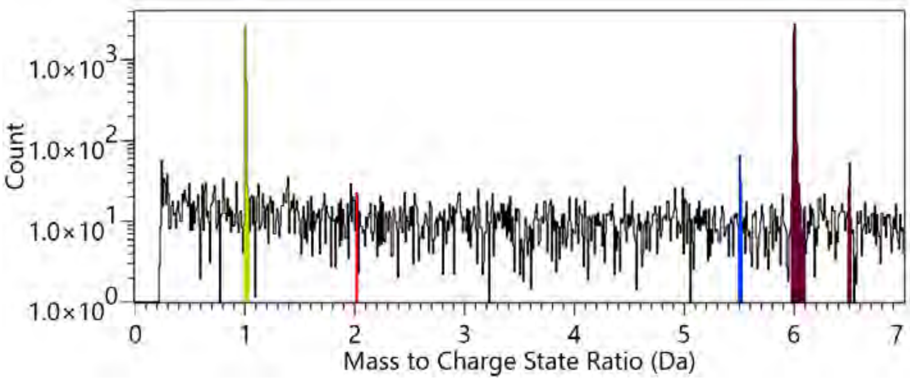

Figure A.3: Background corrected mass spectrum of a quenched Steel-1 specimen up to 7 Da.

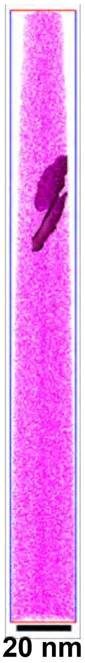

Figure A.4: Overview of a quenched Steel-1 specimen. Showing the measured Fe atoms in pink. The isosurfaces with a concentration of C >8.0 at.% are shown in dark red.

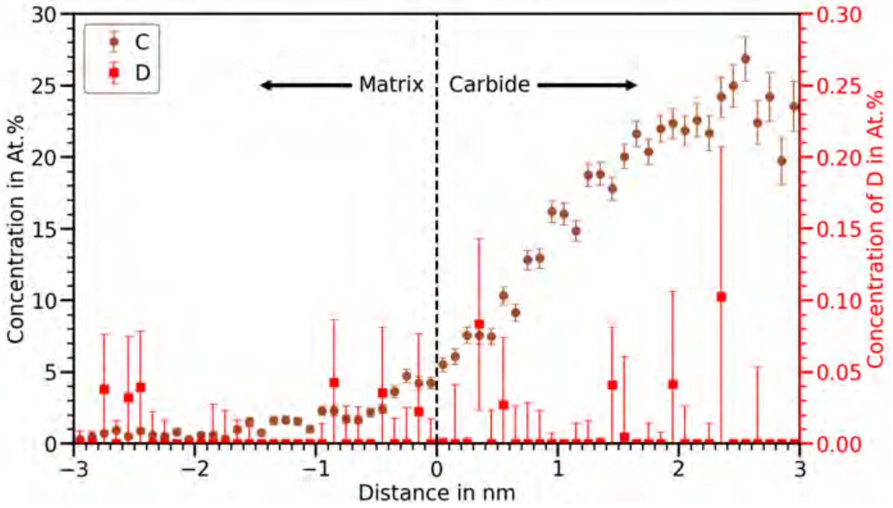

Figure A.5: *Proxigram* of the isosurfaces with a C concentration >8.0 at.%, showing the concentration of C and D as a function of the distance to the isosurface of a quenched Steel-1 specimen.

A.2 Heat Treated Steel-1

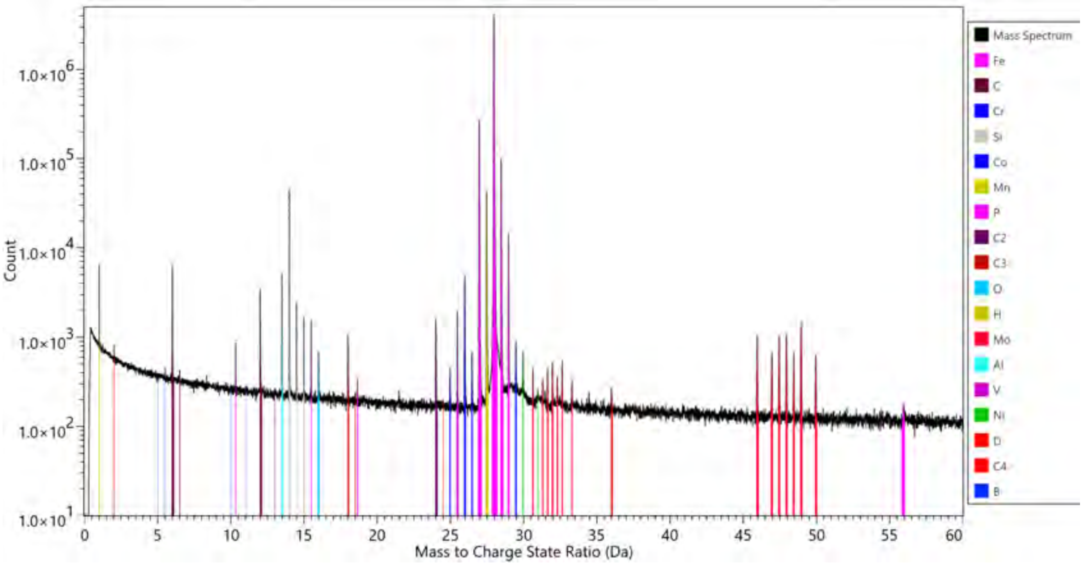

Figure A.6: Indexed mass spectrum of a heat treated Steel-1 specimen.

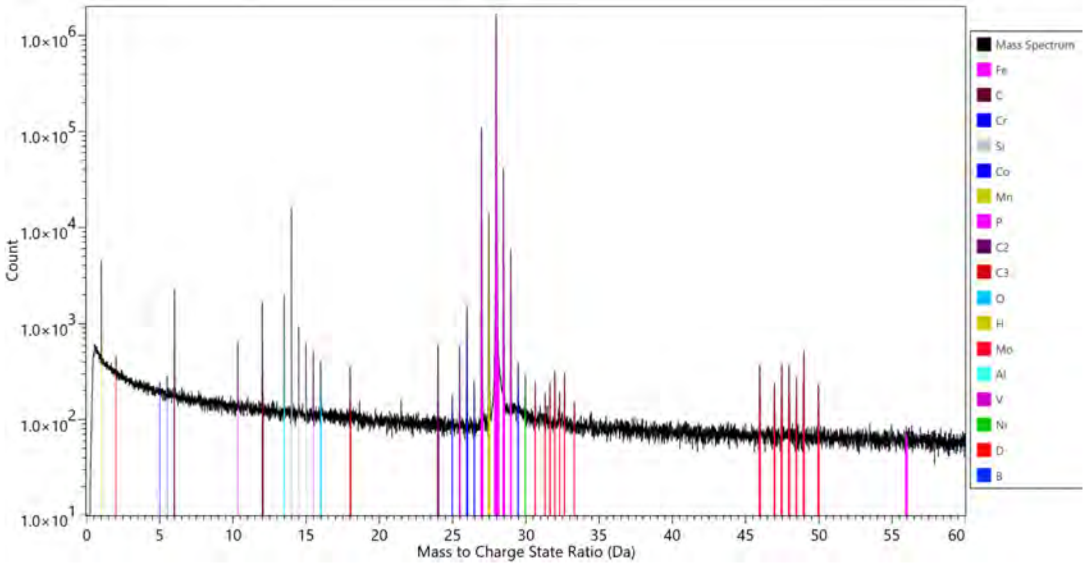

Figure A.7: Indexed mass spectrum of a heat treated Steel-1 specimen.

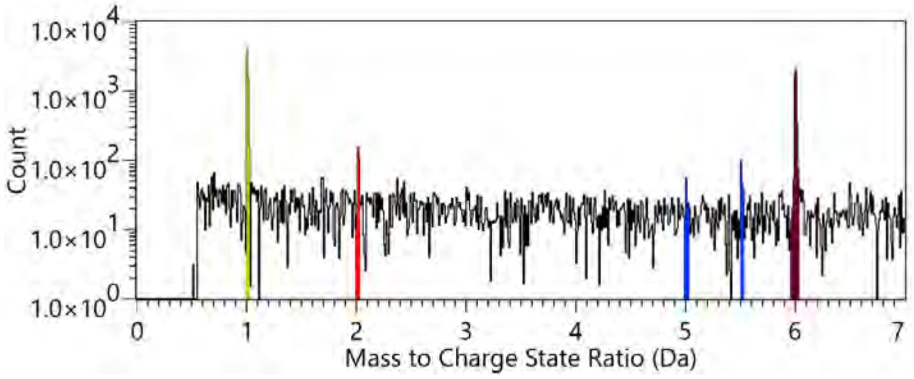

Figure A.8: Background corrected mass spectrum of a heat treated Steel-1 specimen up to 7 Da.

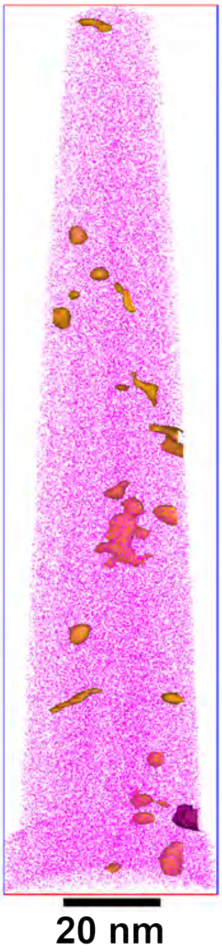

Figure A.9: Overview of a heat treated Steel-1 specimen, showing measured Fe atoms in pink. The isosurfaces with a combined concentration of (C, Mo, V) >3.4 at.% are shown in orange. The isosurfaces with a concentration of C >8.0 at.% are shown in dark red.

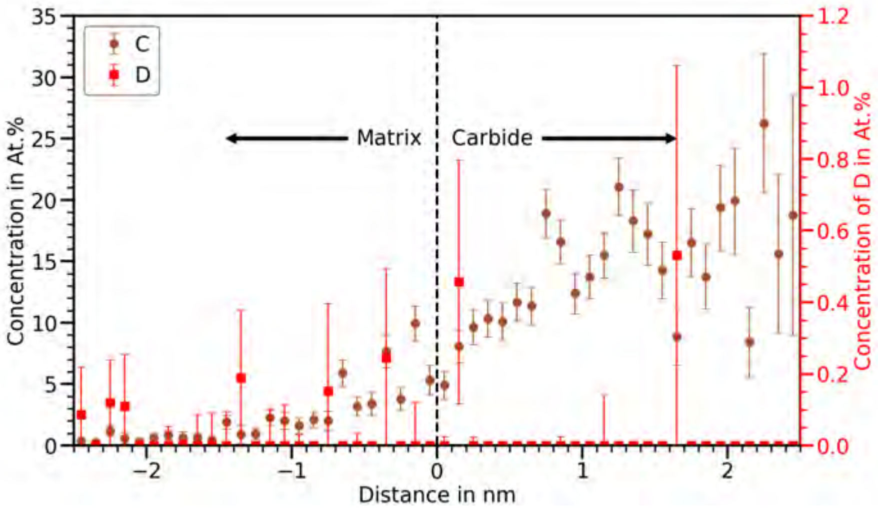

(a)

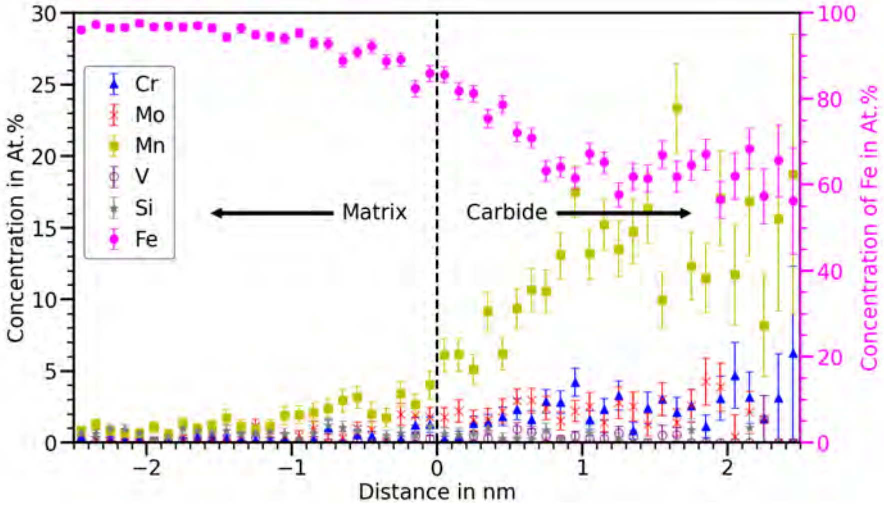

(b)

Figure A.10: *Proxigrams* of the isosurfaces with a concentration of C >8.0 at.%, showing the concentration as a function of the distance to the isosurface of a heat treated Steel-1 specimen: (a) concentration of C and D, and (b) concentration of Cr, Mo, Mn, V, Si, and Fe.

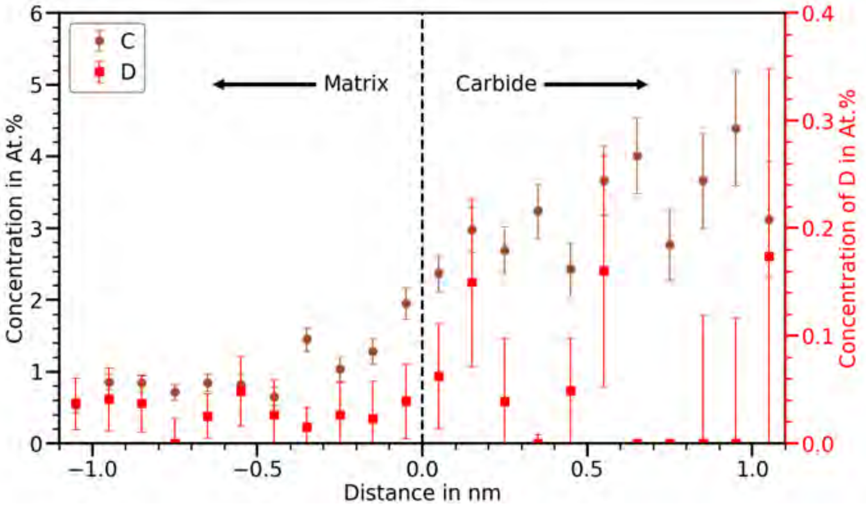

(a)

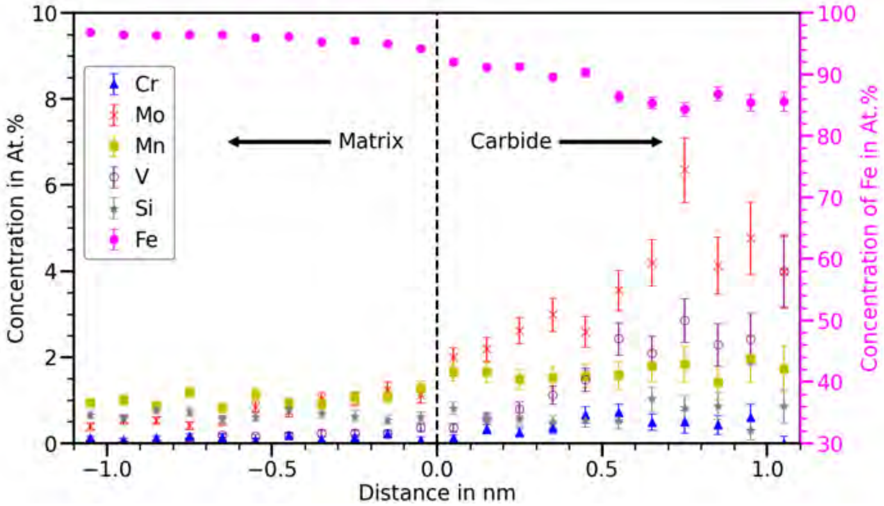

(b)

Figure A.11: *Proxigrams* of the isosurfaces with a combined concentration of (C, Mo, V) >3.4 at.%, showing the concentration as a function of the distance to the isosurface of a heat treated Steel-1 specimen: (a) concentration of C and D, and (b) concentration of Cr, Mo, Mn, V, Si, and Fe.

A.3 V-Steel

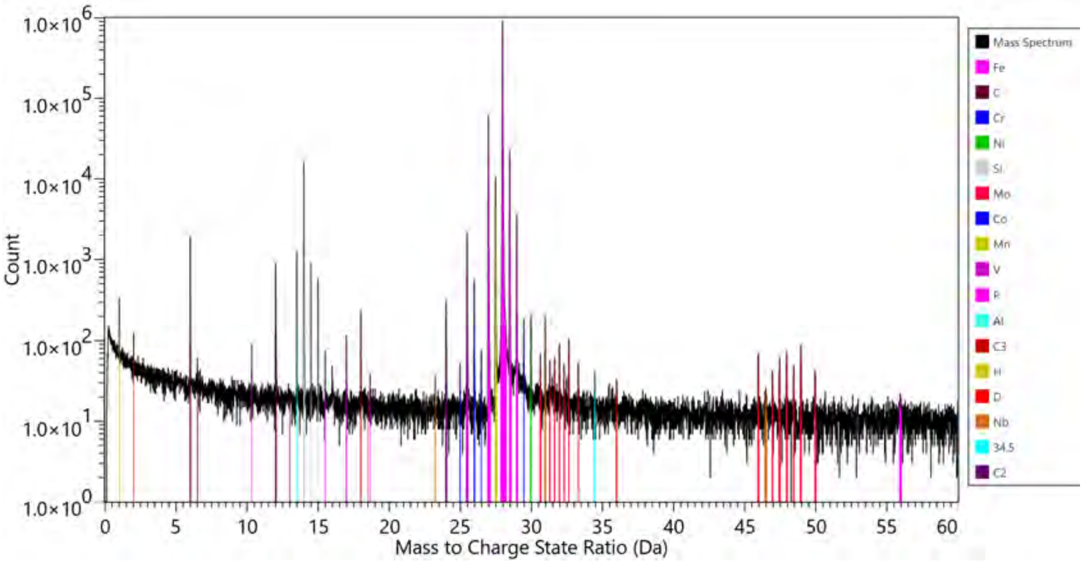

Figure A.12: Indexed mass spectrum of a V-steel specimen.

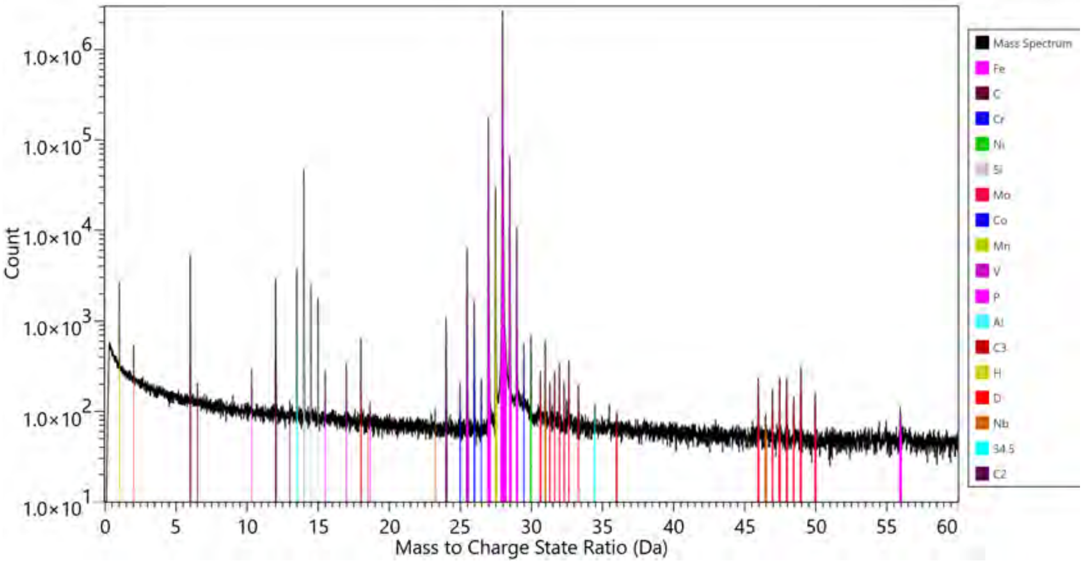

Figure A.13: Indexed mass spectrum of a V-steel specimen.

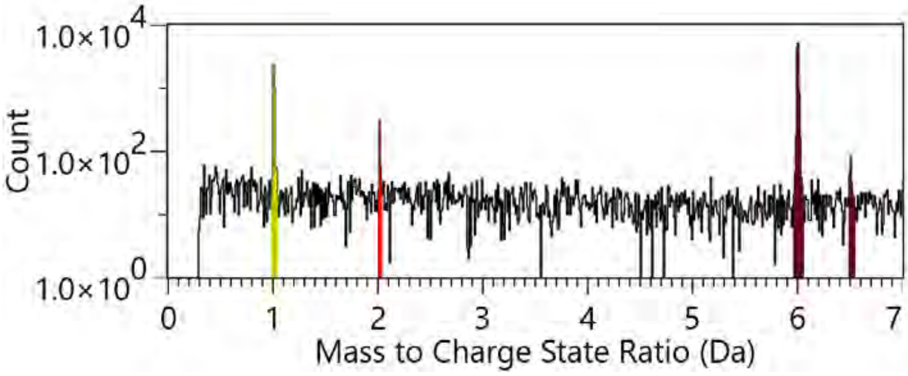

Figure A.14: Background corrected mass spectrum of a V-steel specimen up to 7 Da.

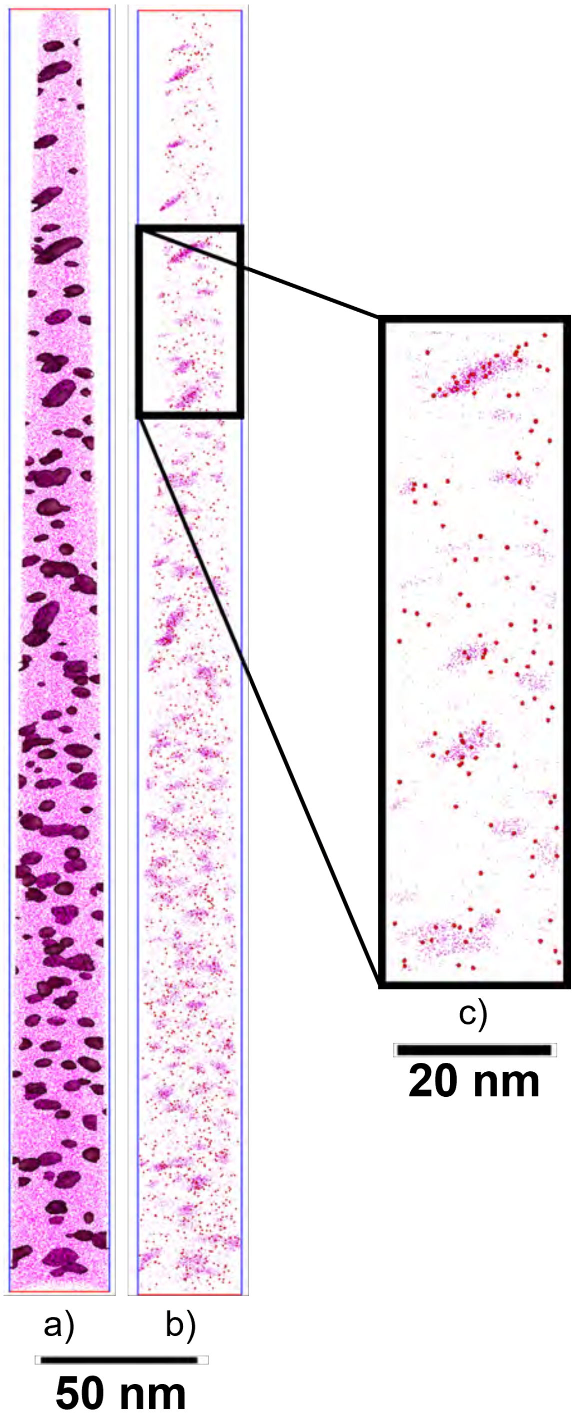

Figure A.15: Overview of a V-steel specimen. Showing in a) the measured Fe atoms in pink. The isosurfaces of a combined concentration of (C, Mo, V) >3.4 at.% are shown in brown. In b), the V (pink) and D (red) atoms of the measurement are shown. In c) a 10 nm thick slice is shown.

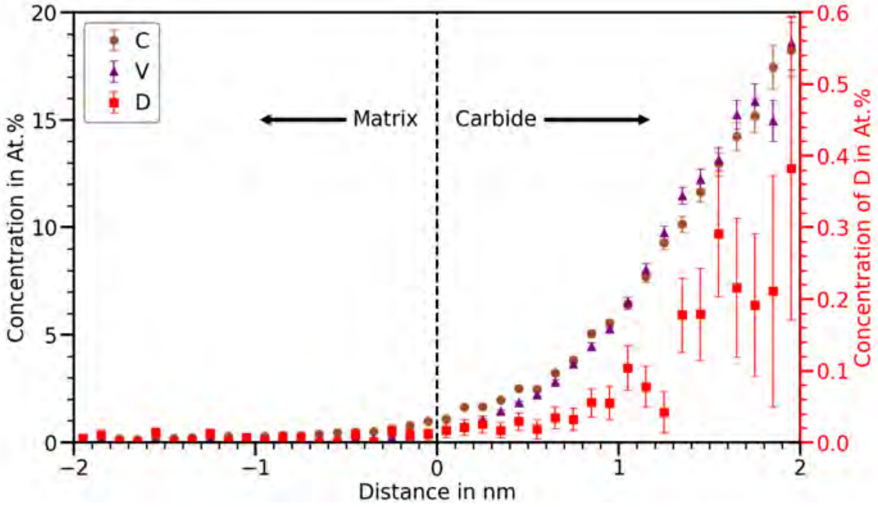

(a)

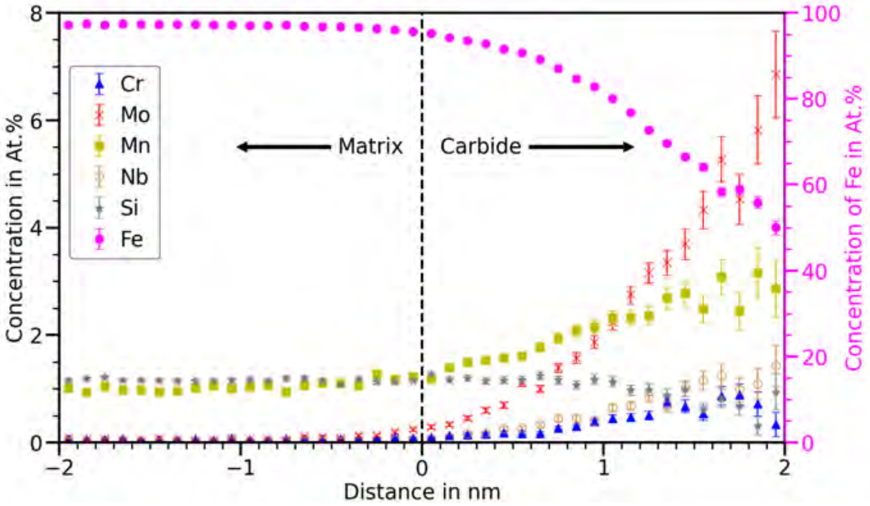

(b)

Figure A.16: *Proxigrams* of the isosurfaces with a combined concentration of (C, Mo, V) >3.4 at.%, showing the concentration as a function of the distance to the isosurface of a V-steel specimen: (a) concentration of C, V, and D, and (b) concentration of Cr, Mo, Mn, Nb, Si, and Fe.

A.4 Ti-Steel

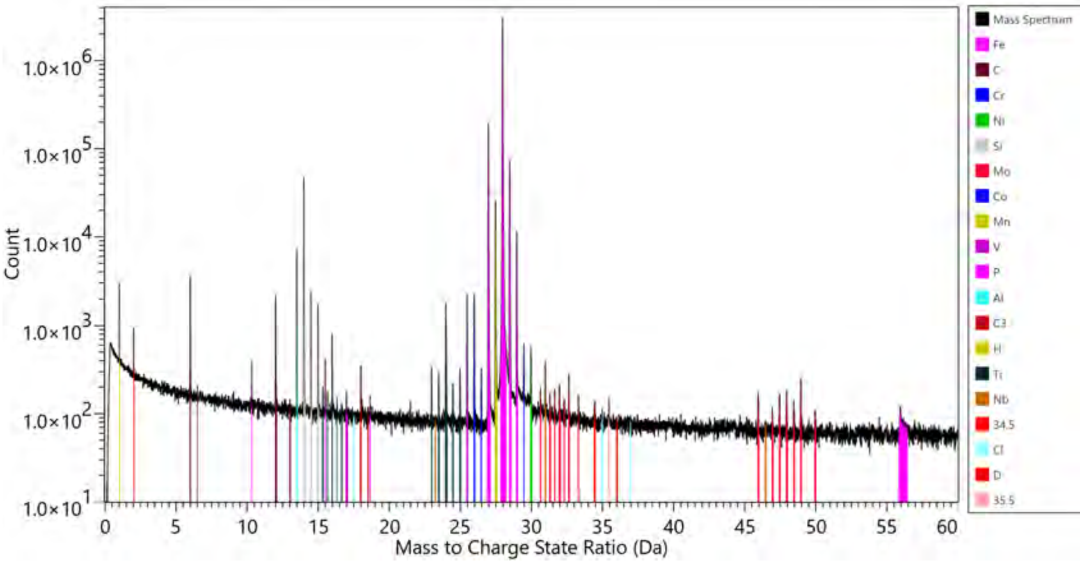

Figure A.17: Indexed mass spectrum of a Ti-steel specimen.

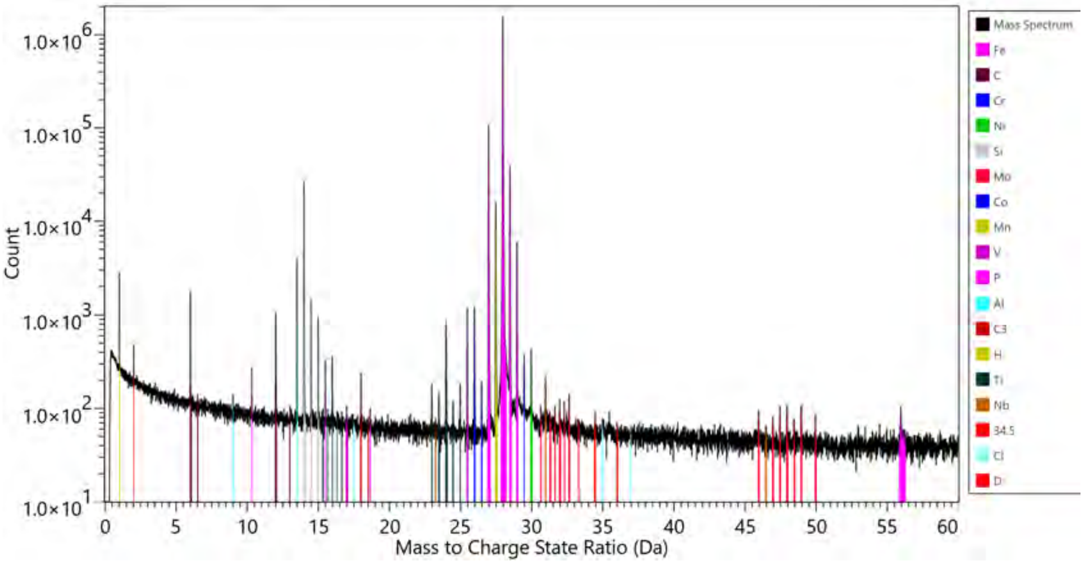

Figure A.18: Indexed mass spectrum of a Ti-steel specimen.

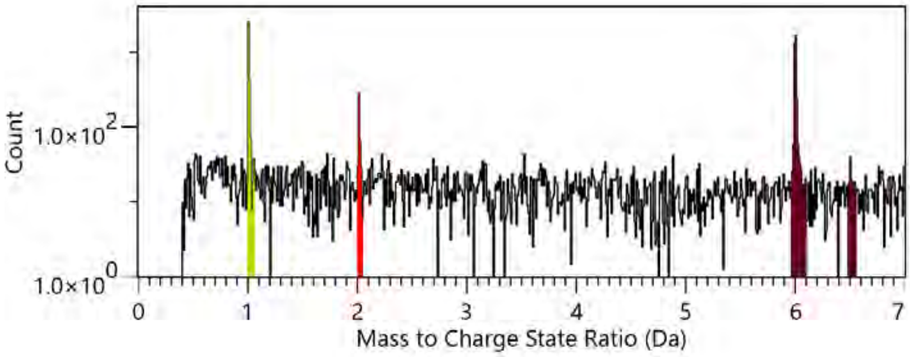

Figure A.19: Background corrected mass spectrum of a Ti-steel specimen up to 7 Da.

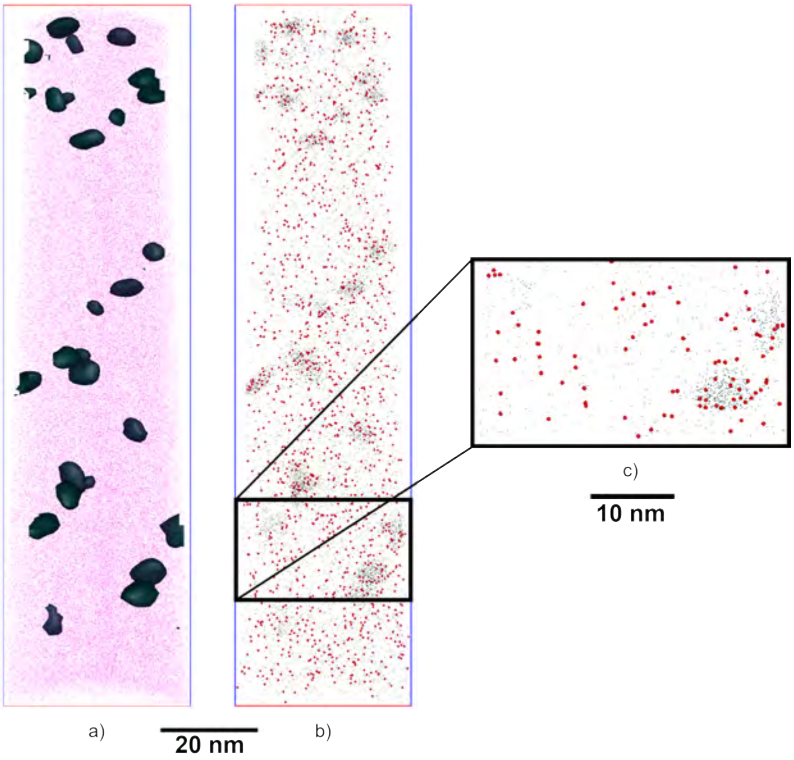

Figure A.20: Overview of a Ti-steel specimen. Showing in a) the measured Fe atoms in pink. The isosurfaces with a Ti-concentration >2.0 at.% are shown in dark green. In b), the Ti (dark green) and D (red) atoms are visualized. In c) a 10 nm tick slice is shown.

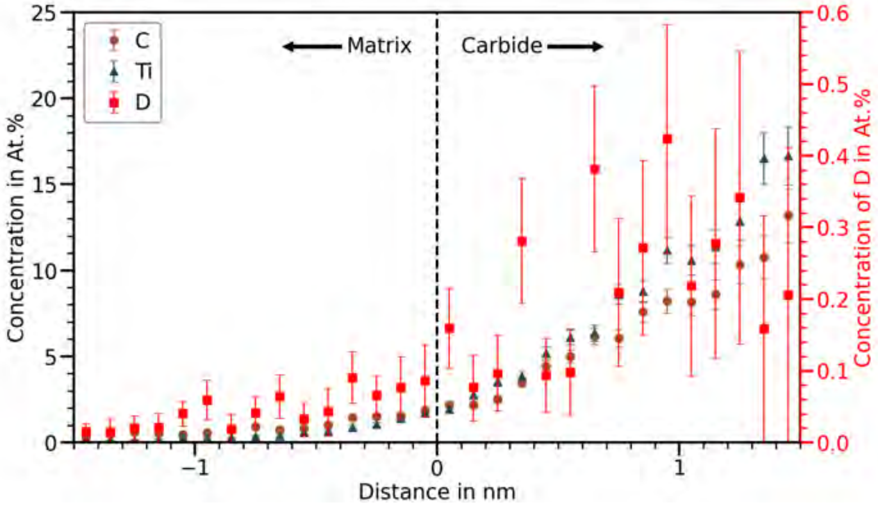

(a)

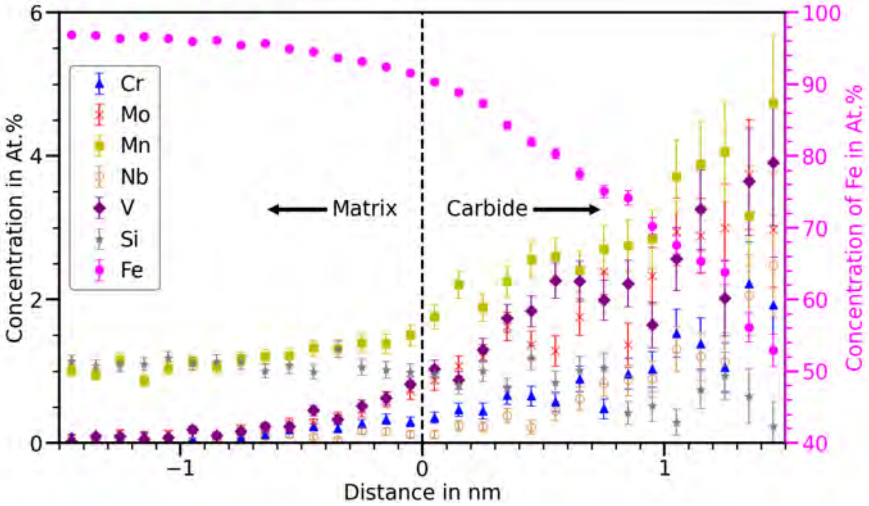

(b)

Figure A.21: *Proxigrams* of the isosurfaces with a concentration of Ti >2.0 at.%, showing the concentration as a function of the distance to the isosurface of a Ti-steel specimen: (a) concentration of C, Ti, and D, and (b) concentration of Cr, Mo, Mn, Nb, V, Si, and Fe.

DEPARTMENT OF PHYSICS
CHALMERS UNIVERSITY OF TECHNOLOGY
Gothenburg, Sweden
www.chalmers.se

CHALMERS
UNIVERSITY OF TECHNOLOGY